SCIENCE ROBOTICS | RESEARCH ARTICLE

HUMAN-ROBOT INTERACTION

A neuromechanics solution for adjustable robot compliance and accuracy

Ignacio Abadía[1]*, Alice Bruel[2], Grégoire Courtine[3], Auke J. Ijspeert[2], Eduardo Ros[1], Niceto R. Luque[1]*

Copyright © 2025 The Authors, some rights reserved; exclusive licensee American Association for the Advancement of Science. No claim to original U.S. Government Works

Robots have to adjust their motor behavior to changing environments and variable task requirements to successfully operate in the real world and physically interact with humans. Thus, robotics strives to enable a broad spectrum of adjustable motor behavior, aiming to mimic the human ability to function in unstructured scenarios. In humans, motor behavior arises from the integrative action of the central nervous system and body biomechanics; motion must be understood from a neuromechanics perspective. Nervous regions such as the cerebellum facilitate learning, adaptation, and coordination of our motor responses, ultimately driven by muscle activation. Muscles, in turn, self-stabilize motion through mechanical viscoelasticity. In addition, the agonist-antagonist arrangement of muscles surrounding joints enables cocontraction, which can be regulated to enhance motion accuracy and adapt joint stiffness, thereby providing impedance modulation and broadening the motor repertoire. Here, we propose a control solution that harnesses neuromechanics to enable adjustable robot motor behavior. Our solution integrates a muscle model that replicates mechanical viscoelasticity and cocontraction together with a cerebellar network providing motor adaptation. The resulting cerebello-muscular controller drives the robot through torque commands in a feedback control loop. Changes in cocontraction modify the muscle dynamics, and the cerebellum provides motor adaptation without relying on prior analytical solutions, driving the robot in different motor tasks, including payload perturbations and operation across unknown terrains. Experimental results show that cocontraction modulates robot stiffness, performance accuracy, and robustness against external perturbations. Through cocontraction modulation, our cerebello-muscular torque controller enables a broad spectrum of robot motor behavior.

Downloaded from https://www.science.org at The Hong Kong University of Science and Technology (Guangzhou) on May 25, 2026

INTRODUCTION

Robotics development is pursuing autonomous intelligent robots able to dynamically adapt their motor behavior to the environment and task requirements (*1*). Traditional industrial robots are designed for specific tasks and controlled, structured environments, prioritizing performance accuracy and operation speed. Nevertheless, robotics applications are expanding beyond manufacturing plants into the real world, defining new applications that involve collaboration through physical human-robot interaction (HRI). The evolving constraints of physical HRI require these collaborative robots to change their priorities over time, thus demanding adjustable motor behavior. For example, assistive robots must not only perform motor tasks accurately and discern objects by their fragility for delicate manipulation but also allow the human to freely drive their motion if required; rehabilitation robots must adapt to the evolution of the patient's abilities (*2*). Even a seemingly simple task as an object handover involves different phases that require both the giver and receiver to dynamically adapt their behavior (*3*); when receiving a tool from a human, the robot motion should be soft when approaching the tool to not destabilize or compromise the human's safety, whereas the subsequent task execution using the tool demands more robustness from the robot. Thus, the range of tasks and environments encountered by collaborative robots requires them to adaptively transition between robust and softer, compliant motor behavior depending on the circumstances.

These motor requirements arise from the deployment of robots in the unstructured real world and can be addressed by developing robots that mimic the living organisms that inhabit it (*4*). In nature, adaptive motor behavior is facilitated by the central nervous system (CNS). Robotics has thus looked to neuroscience to develop brain-inspired technologies that endow robots with some sort of biomimetic behavior (*5*): generalization to unseen scenarios (*6*), precise navigation (*7*), multitasking (*8*), adaptation to changes in dynamics (*9*), or robustness against nondeterministic time delays (*10*). However, motor behavior is not shaped exclusively by what occurs inside the brain; it is also substantially influenced by body biomechanics (*11*, *12*). This is exemplified by the passive-dynamics walker robots, in which mechanical properties enable stable locomotion with minimal actuation and rather primitive control (*13*). Consequently, robotics also looks to biomechanics to incorporate and harness some of its inherent features: agile locomotion across different terrains (*14*); variable stiffness actuators (*15*); adhesive behavior to diverse surfaces (*16*); or the lifelike capabilities to change shape, modulate stiffness, self-heal, or grow, qualities that soft robotics aims to replicate (*17*). Therefore, combining brain-inspired and biomechanics solutions will foster the development of robots with ever more biomimetic behavior.

The versatility of human motor behavior very well reflects this interaction between neural control and body morphology. For instance, our distinctive hand dexterity, crucial for precise and adaptive manipulation, emerges from the synergy of the CNS and biomechanics (*18*). Actually, our physical interactions with the world are mainly mediated through the upper limbs, whose functionality is directly linked to their morphology (*19*). The human upper limb is actuated by no fewer than 20 muscles that control seven degrees of freedom (DOFs) (three DOFs in the shoulder, two in the elbow, and two in the wrist,

---

[1]Research Center for Information and Communication Technologies, Department of Computer Engineering, Automation and Robotics, University of Granada, Granada, Spain. [2]Biorobotics Laboratory, École Polytechnique Fédérale de Lausanne (EPFL), Lausanne, Switzerland. [3]NeuroX Institute and .NeuroRestore, EPFL/CHUV/UNIL, Lausanne, Switzerland.
*Corresponding author. Email: iabadia@ugr.es (I.A.); nluque@ugr.es (N.R.L.)

excluding the hand DOF) (*20*). This muscle redundancy and overactuation add to the complexity of musculoskeletal dynamics, which are already sophisticated because of the nonlinear properties of muscles, tendons, and other soft tissues (*21*). Such dynamic intricacy requires fine control mechanisms in the CNS to govern motion, but at the same time, muscle actuation offers inherent benefits. Nonlinear muscle viscoelasticity induces self-stability (*22*, *23*), provides an intrinsic zero-delay response to perturbations (*24*), and simplifies neuronal information processing by off-loading computation to the morphological structure (*25*–*27*). Furthermore, muscle passive viscoelasticity can be actively controlled to modify behavior (*12*). Apart from these intrinsic mechanical properties, the arrangement of agonist-antagonist muscle groups to actuate joints enables cocontraction: the simultaneous activation of antagonistic muscles surrounding a joint. Cocontraction can be actively modulated to increase performance accuracy, regulate joint stiffness, and, thereby, modify the dynamic response to perturbations, thus broadening the motor repertoire (*28*–*30*).

These muscle mechanical properties and their agonist-antagonist distribution have inspired new robotic actuators (*15*, *31*–*34*); the challenges of performing in unstructured environments can be approached from a hardware perspective that mimics functional biological tissues (*35*). Nonetheless, hardware-based solutions face manufacturing challenges and are often limited to specific platforms, which can constrain their wide-scale adoption (*1*, *35*, *36*), and introducing nonlinear dynamics complicates accurate and reliable control (*37*).

Besides hardware implementations, biological tissue can also inspire software-based control approaches. Muscle redundancies, viscoelasticity, and cocontraction inspired impedance control (*38*–*40*), which was developed to regulate the dynamic interactions between a manipulator and its environment. Impedance control posits that, when two physical systems interact, one must physically complement the other: If one system behaves as an impedance (accepts motion inputs and yields force outputs), then the other must be an admittance (accepts force inputs and yields a motion response). In its original conception, this control paradigm considers the environment as an admittance given that it can always be pushed upon but does not always move. Hence, the manipulator is considered an impedance for complementarity, reflecting the causality from detected motion to applied force (*39*, *40*). Impedance control can be implemented to maintain a specific impedance across interactions or to regulate and adjust the impedance of the robot depending on the encountered circumstances through variable impedance control (*41*, *42*).

Impedance control implementations depend on well-designed control laws addressing the robot dynamics, a complex issue without a straightforward solution for nonlinear robots, and the desired impedance model, which depends on the environment and task requirements (*41*). In unstructured scenarios, the environment properties are unknown; thus, reliable measurements of the contact force between the robot and the environment are usually required to model the desired impedance (*43*). Consequently, impedance control often relies on extensive analytical development, including robot dynamics, desired impedance, environment information, and/or specialized hardware for sensing capabilities. Both control-based and learning-based approaches have been developed to achieve variable impedance control, but the limitations imposed by their technical requirements reduce their applicability and spread as broad robotic solutions (*42*).

The ultimate goal of impedance control lies in adjusting the dynamic behavior of the robot (*44*). Anthropomorphic solutions can facilitate this achievement. To reduce dependency on reliable sensory feedback, humans adjust their interactions with the environment by regulating limb stiffness (*45*). Rather than directly controlling the force exerted on physical objects, modulating limb stiffness through muscle cocontraction allows active regulation of our interactions, without prior knowledge about the environment and without accurate modeling information.

Inspired from these biological features, we model muscle mechanical properties and include them in a robot torque controller. We replicate muscle viscoelasticity and agonist-antagonist actuation, drawing from Ekeberg's computational muscle model (*46*), a model previously applied to study animal locomotion (*47*), and robust undulatory swimming in robots (*48*). We expand the muscle model by incorporating tunable cocontraction and a spinal cord (SC) reflex mechanism and apply it to six DOFs of the Baxter robot arm (*49*), performing different motor tasks: continuous trajectories at different speeds, external perturbations, and operation across different terrains. By adjusting muscle cocontraction, which also modulates the SC-based reflex, we can regulate robot stiffness, performance accuracy, and the response to interactions. Thus, we achieve muscle-like actuation using electric motors without needing antagonistic actuators. We also integrate a cerebellar spiking neural network (SNN) to control the muscle dynamics and drive the robot toward its motor goal. The cerebellum, key for biological motor control and learning (*50*–*54*), has previously been validated for robot control (*9*, *10*); however, these previous implementations lacked motor behavior regulation. In the current implementation, the cerebellar SNN generates high-level muscle activation signals, in contrast with previous implementations of muscle dynamics in robots, which typically relied on oscillatory activation signals (*48*, *55*). Subsequently, the muscle dynamics generates the joint torque signals that drive the robot motion. The cerebellar SNN is equipped with synaptic plasticity, allowing motor adaptation to control the unknown plant dynamics without prior analytical knowledge, that is, model-free control because both the muscle and robot dynamics are initially unknown to the cerebellum.

Here, we propose a neuromechanics approach for adjustable robot motor behavior (Fig. 1). By harnessing muscle dynamics and cerebellar adaptability, our approach achieves adjustable motor behavior through the regulation of the robot stiffness, without prior analytical modeling (model-free), without environment information and hence applicable to unknown environments, and without contact force sensing or specific hardware given that it relies on only position sensory feedback. By integrating brain-inspired and biomechanics solutions, our cerebello-muscular torque controller enables the adjustment of the robot motor behavior, striking a dynamic trade-off between performance accuracy and compliance: high accuracy and robustness against perturbations versus adopting lower accuracy and softer, compliant behavior in response to interactions.

RESULTS

Integration of a cerebellar model, muscle dynamics, and a robot

We implemented a cerebellar SNN and a software-based muscle model, both combined to build a cerebello-muscular torque controller operating within a feedback control loop with the Baxter robot as the

Downloaded from https://www.science.org at The Hong Kong University of Science and Technology (Guangzhou) on May 25, 2026

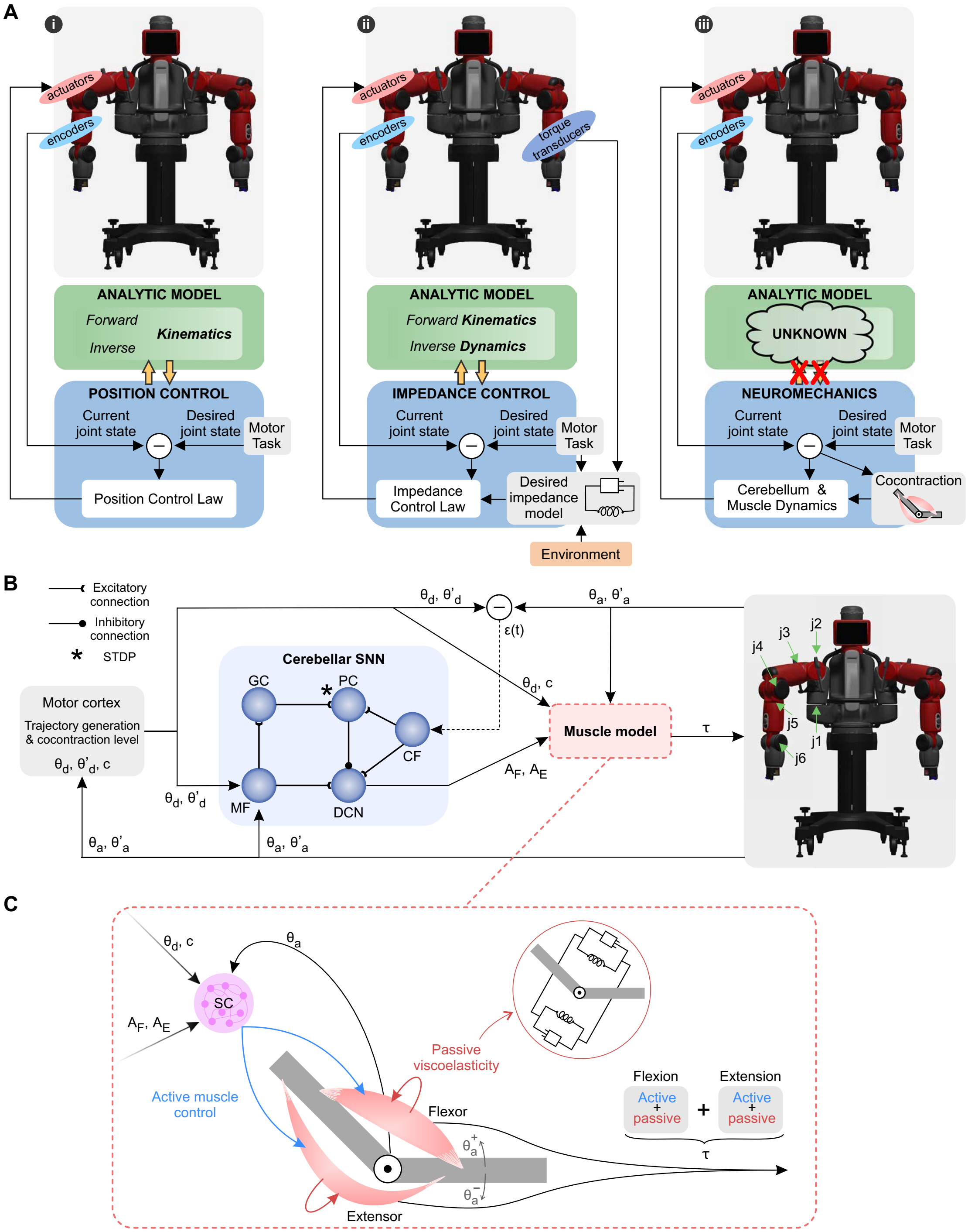

Fig. 1. Neuromechanics robot control for adjustable motor behavior. (**A**) Different control approaches. (i) Encoder-based position control uses position data from encoders and requires kinematic models; suitable for position tracking but limited for dynamic interactions. (ii) Torque transducer-based impedance control uses torque transducers or contact force sensors to measure and control interaction forces/torques assisted by dynamic models; effective for adaptive behavior but requires complex modeling and control. (iii) Neuromechanics encoder-based torque control uses muscular and cerebellar mechanisms to control torque using position feedback; adjustable compliance and accuracy without kinematic or dynamic models (model-free), effective in unknown terrains. (**B**) Cerebello-muscular control loop. The motor task was defined as desired joint coordinates (position θ_d and velocity θ'_d) to be tracked. A module representing the motor cortex provides the desired coordinates and cocontraction level (*c*). The cerebellar SNN receives, through MFs, the sensory input comprising the desired and actual (θ_a and θ'_a) joint coordinates and, through CFs, the instructive signal (ε). Activity from the deep cerebellar nuclei (DCN) layer delivers flexion-extension activation commands (A_F and A_E) to the muscle model, which also receives θ_d, *c*, θ_a, and θ'_a as sensory input and generates joint torque commands (τ) to drive the robot. Control loop operating at 500 Hz. (**C**) Schematic of the muscle model. Active and passive components are integrated: the cerebellar A_F and A_E commands and a spinal cord (SC) reflex actively drive the robot behavior; passive mechanical viscoelasticity adds to the output torque. Muscle viscoelasticity schematic inspired from (*46*).

Downloaded from https://www.science.org at The Hong Kong University of Science and Technology (Guangzhou) on May 25, 2026

front-end body (Fig. 1, B and C). The cerebellar network adapted the motor commands needed to perform different tasks involving six DOFs, where each robot DOF was governed by the dynamics of the implemented muscle model, in addition to Baxter built-in series elastic actuators (*49*). The cerebellar network, built on previous works (*9*, *10*, *56*), used the following sensory inputs: joint coordinates describing the desired trajectory for the motor task (position θ_d and velocity θ'_d), actual joint coordinates of the robot (position θ_a and velocity θ'_a), and an instructive signal (ε) computing the mismatch between the desired and actual joint states. On the basis of this input sensory information, the cerebellar network generated the agonist and antagonist muscle activation commands (A_F for flexion and A_E for extension per joint), which were then sent to the muscle model. Our muscle model, derived from (*46*), simulated a pair of antagonistic muscles and was developed to include adjustable cocontraction (c) and a reflex component on the basis of SC circuitry. Hence, each robot joint had its corresponding muscle model that simulated an agonist-antagonist muscle pair and included the following: active control of agonist-antagonist dynamics (flexion-extension, commanded by the cerebellar signals A_F and A_E), cocontraction level, an SC-based reflex response (R_{SC}), and passive viscoelastic properties. The combination of the different muscular components produced a torque signal per joint (τ), which was then sent to the robot, thus closing the feedback loop. The desired joint coordinates and the adjustable cocontraction level were fed into the loop by a module representing motor cortex functionality (*57*–*60*). For a comprehensive description of the muscle model, the cerebellar SNN, and the robot, see Materials and Methods.

To adjust the robot motor behavior, we modified the muscle dynamics by varying the cocontraction value (c), affecting both the active and passive muscle properties (see Materials and Methods). To explore a rich spectrum of robot behavior, we conducted tests within a wide cocontraction range: $c = [x0, x1, x3, x5, x7, x9, x10]$, where *x0* corresponds to $c = 0.0$, *x1* is $c = 0.1$, *x3* is $c = 0.3$, and so on. The following sections detail our cerebello-muscular torque controller performing with different cocontraction levels and its effect on key tenets of HRI: performance accuracy, torque response, and reaction against external perturbations (soft versus robust behavior). An overview of our neuromechanics approach is shown in Movie 1.

Enhancement of performance accuracy through cocontraction

First, we assessed the influence of cocontraction on performance accuracy. Two motor tasks constituted our motor control benchmark: a circular trajectory executed in the vertical plane and a figure-eight trajectory executed in the horizontal plane. Each task was performed in 2.5 s; for the desired joint coordinates specific to each motor task, see the Supplementary Materials (fig. S1). For each cocontraction value tested, the cerebello-muscular controller underwent 1000 consecutive trials of the trajectory. The trial-and-error cerebellar learning process started without prior knowledge of the plant dynamics, and as cerebellar adaptation progressed, it allowed operation of the given muscle dynamics to command the robot in the execution of the motor tasks, leading to a gradual reduction in the performance error (Fig. 2, A and B). As the motor adaptation process concluded, our cerebello-muscular torque controller accurately tracked the desired joint positions (Fig. 2, C and D).

Movie 1. Overview of the neuromechanics approach.

Increased cocontraction levels correlated with a more consistent execution of the motor task as the trajectory variability decreased (Fig. 2, E and F), demonstrating a significant enhancement in performance accuracy measured as the position mean absolute error (MAE) (Fig. 2, G and H). For all cocontraction values, the performance improved the reference provided by the factory-default position controller. Nevertheless, it was observed that increasing cocontraction did not yield an endless enhancement of performance accuracy; the highest cocontraction values (*x10* for the circular trajectory; *x9* and *x10* for the figure-eight trajectory) did not significantly reduce the error beyond that achieved by preceding cocontraction values.

Enhancement of performance accuracy through cocontraction is limited by motion speed

Previous studies have reported that, biologically, cocontraction stabilizes the upper limb and enhances motion accuracy (*61*, *62*); however, its benefits diminish during high-speed ballistic movements, which become spastic in the presence of cocontraction (*63*). To test whether these findings still apply to our robotic setup, we evaluated the influence of cocontraction on performance accuracy when increasing the motion speed. We extended the original motor benchmark by testing the following trajectory durations: a vertical circle performed in 2.5, 2.0, 1.5, 1.0, and 0.8 s; a horizontal figure-eight trajectory performed in 2.5 and 2.0 s. Note that the figure-eight trajectory performed in 2.0 s forced the joint speed close to the hardware limitations specified by the robot manufacturer, thus preventing further increments in speed of the figure-eight trajectory for safety reasons. For a description of the joint coordinates of each motor task performed at different speeds, see the Supplementary Materials (fig. S1).

For the slower executions of the circular trajectory (2.5, 2.0, and 1.5 s), increasing cocontraction improved the performance accuracy, except for the highest cocontraction value (*x10*) in the 2.5- and 1.5-s trajectories and for cocontraction *x9* in the 2.0-s trajectory, which did not significantly modify the tracking error (Fig. 3A). Conversely, for faster trajectories (1.0 and 0.8 s), the highest cocontraction value (*x10*) did not enhance but significantly worsened the trajectory execution. This deterioration was already noticeable with the cocontraction value *x7* for the fastest trajectory (Fig. 3A). Regarding the figure-eight trajectory, previous observations showed that, for the slowest trajectory (2.5 s), the cocontraction values *x9* and *x10* did not significantly affect the trajectory tracking. For the fastest trajectory (2.0 s), we observed that the cocontraction value *x5* significantly increased the tracking error compared with the immediately lower cocontraction value and that higher values did not further modify performance accuracy (Fig. 3B).

Downloaded from https://www.science.org at The Hong Kong University of Science and Technology (Guangzhou) on May 25, 2026

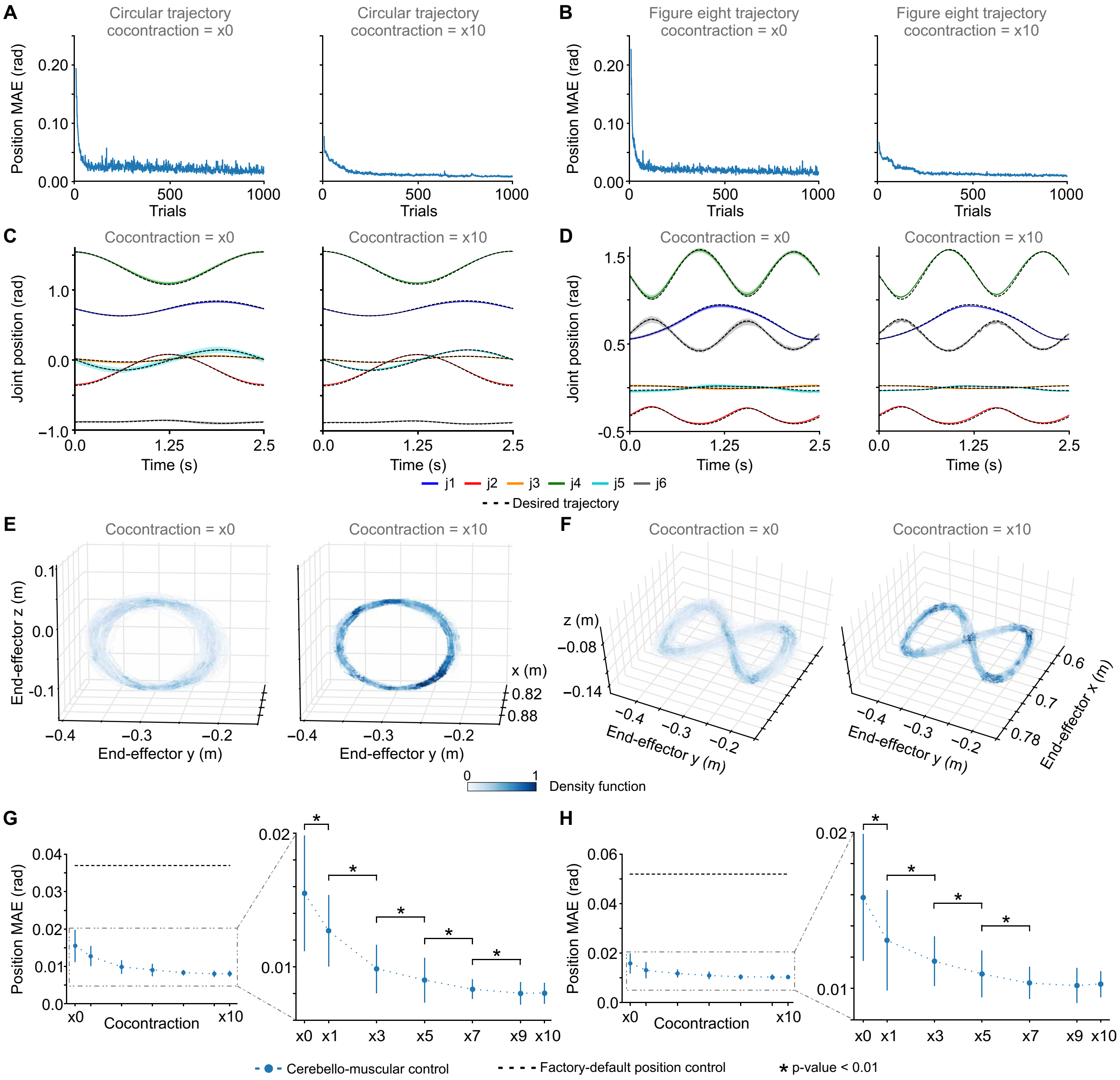

Fig. 2. Cocontraction effect on performance accuracy. (**A**) Position MAE evolution during cerebellar motor adaptation for the circular and (**B**) figure-eight trajectories with the lowest and highest cocontraction values. (**C**) Tracking of desired joint position coordinates for the circular and (**D**) figure-eight trajectories with the lowest and highest cocontraction values. Lines show the mean, and shading shows the SD per time step of the last 100 trials of motor adaptation ($n = 100$). (**E**) Cartesian space representation of the robot end-effector trajectory with the lowest and highest cocontraction values for the circular and (**F**) figure-eight trajectories. The density function over the last 100 trials of the motor adaptation process is shown. (**G**) Position MAE per trial; data show the mean, and error bars show the SD of the final 100 trials ($n = 100$) performed by the cerebello-muscular controller under each cocontraction value for the circular and (**H**) figure-eight trajectories. Consecutive cocontraction values were compared using Welch's *t* test. The performance of the factory-default position control is included for reference. Dashed lines in (G) and (H) were added to cerebello-muscular data as guides to the eye.

Downloaded from https://www.science.org at The Hong Kong University of Science and Technology (Guangzhou) on May 25, 2026

Muscle torque modifications induced by cocontraction

The joint torque commanded to the robot was given by the output of the muscle dynamics. Varying the cocontraction value modified the muscle dynamics (see Materials and Methods), thereby affecting the output muscle torque (Fig. 4A and fig. S2 for the circular trajectory and fig. S3 for the figure-eight trajectory). To assess the torque changes induced by cocontraction, we computed the joint torque-time integral (TTI) as a measurement of the delivered energy (*64*), a metric also used in neuromuscular studies to account for the ability to maintain force over time (*65–67*). This involved calculating the integral of the joint torque over the motor task duration (2.5 s for both the circular and figure-eight trajectories; see Materials and Methods). Although statistically significant variations were observed for certain joints (Fig. 4B), the overall joint TTI change was relatively small; the maximum TTI increment across all cocontraction values was 0.24 Nm·s for joint j1 in the circular trajectory and 1.18 Nm·s for joint j2 in the figure-eight trajectory (see Fig. 1B and fig. S12 for joint labels). As a reference for joint torque magnitudes, the robot manufacturer specifies a maximum torque of 50 Nm for joints j1, j2, j3, and j4 and 15 Nm for joints j5 and j6.

To provide deeper insight into the torque response, we broke down the output muscle torque into its different muscle dynamics components and measured the corresponding time integral. According to biological plausibility, the final muscle torque resulted from the interplay of both active and passive components of the muscle dynamics. The cerebellum actively controlled the flexion-extension direction of movement (Fig. 4C), which experienced a maximum time-integral increment across all cocontraction values of 2.27 Nm·s (joint j1) for the circular trajectory and 1.90 Nm·s (joint j4) for the figure-eight trajectory (Fig. 4D). The SC-based reflex component corrected deviations from the desired trajectory, exhibiting an increase with cocontraction (Fig. 4E). The maximum time-integral increment across all cocontraction values was 2.66 Nm·s (joint j2) for the circular trajectory and 3.59 Nm·s (joint j4) for the figure-eight trajectory (Fig. 4F). On the passive side of the muscle dynamics, we considered two components accounting for the muscle mechanical elasticity and viscosity, respectively. The elastic component exhibited an increase with cocontraction (Fig. 4G), showing a peak increment of 3.68 Nm·s (joint j1) for the circular trajectory and 3.71 Nm·s (joint j1) for the figure-eight trajectory (Fig. 4H). Conversely, the viscous component exhibited relatively smaller variations with cocontraction changes (Fig. 4I), showing a peak increment across all cocontraction values of 0.04 Nm·s (joint j6) for the circular trajectory and 0.21 Nm·s (joint j6) for the figure-eight trajectory (Fig. 4J). The changes induced by cocontraction to the different components of the muscle dynamics were compensatory: When combining all components to generate the output muscle torque, the time-integral changes were mitigated; all muscular components, except the viscous one, exhibited higher time-integral changes than the resulting output muscle torque.

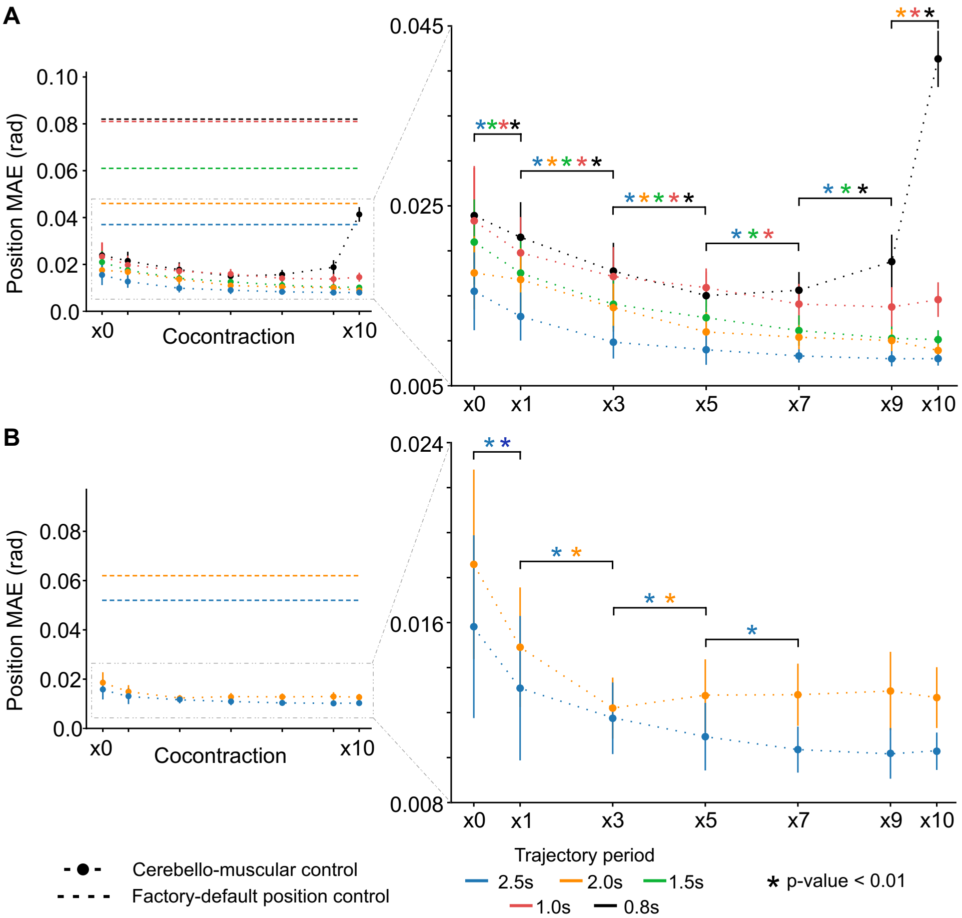

Fig. 3. Cocontraction effect on performance accuracy at different motion speeds. (**A**) Position MAE per trial for the cerebello-muscular controller under each cocontraction value performing the circular trajectory at different speeds: trajectory durations of 2.5, 2.0, 1.5, 1.0, and 0.8 s, and (**B**) figure-eight trajectory at different speeds: trajectory durations of 2.5 and 2.0 s. Data show the mean, and error bars show the SD over the final 100 trials ($n = 100$) of the motor adaptation process. Consecutive cocontraction values were compared using Welch's *t* test. Dashed lines were added to cerebello-muscular data as guides to the eye.

Enhancing robot physical agency through cocontraction: Response to external perturbations

After analyzing the influence of cocontraction on performance accuracy, we investigated its influence on robot behavior when reacting to external perturbations. Once motor adaptation had been settled, we attached a payload to the end effector during the execution of the motor tasks and measured the deviation in trajectory tracking for each cocontraction value. We used a 0.5-kg payload for the circular trajectory (Fig. 5) and a 1-kg payload for the figure-eight trajectory (fig. S4). To obtain a precise measurement of the payload-induced deviation and to isolate the role of cocontraction, we initially disabled cerebellar synaptic plasticity, thus preventing cerebellar adaptation to dynamic changes and inhibiting convergent behavior (*9*). Hence, the payload effect remained over time, and the perturbation response could only be attributed to the cocontraction level, providing a comprehensive assessment of the performance variations (before and after payload attachment) for each cocontraction value (Fig. 5A and fig. S4A). We observed that, as cocontraction increased, the robot motor response exhibited greater robustness to perturbations; higher cocontraction values resulted in smaller deviations when attaching the payload. In accordance with biological motor behavior, a direct relation between cocontraction and limb stiffness was found. We measured the limb stiffness as

Downloaded from https://www.science.org at The Hong Kong University of Science and Technology (Guangzhou) on May 25, 2026

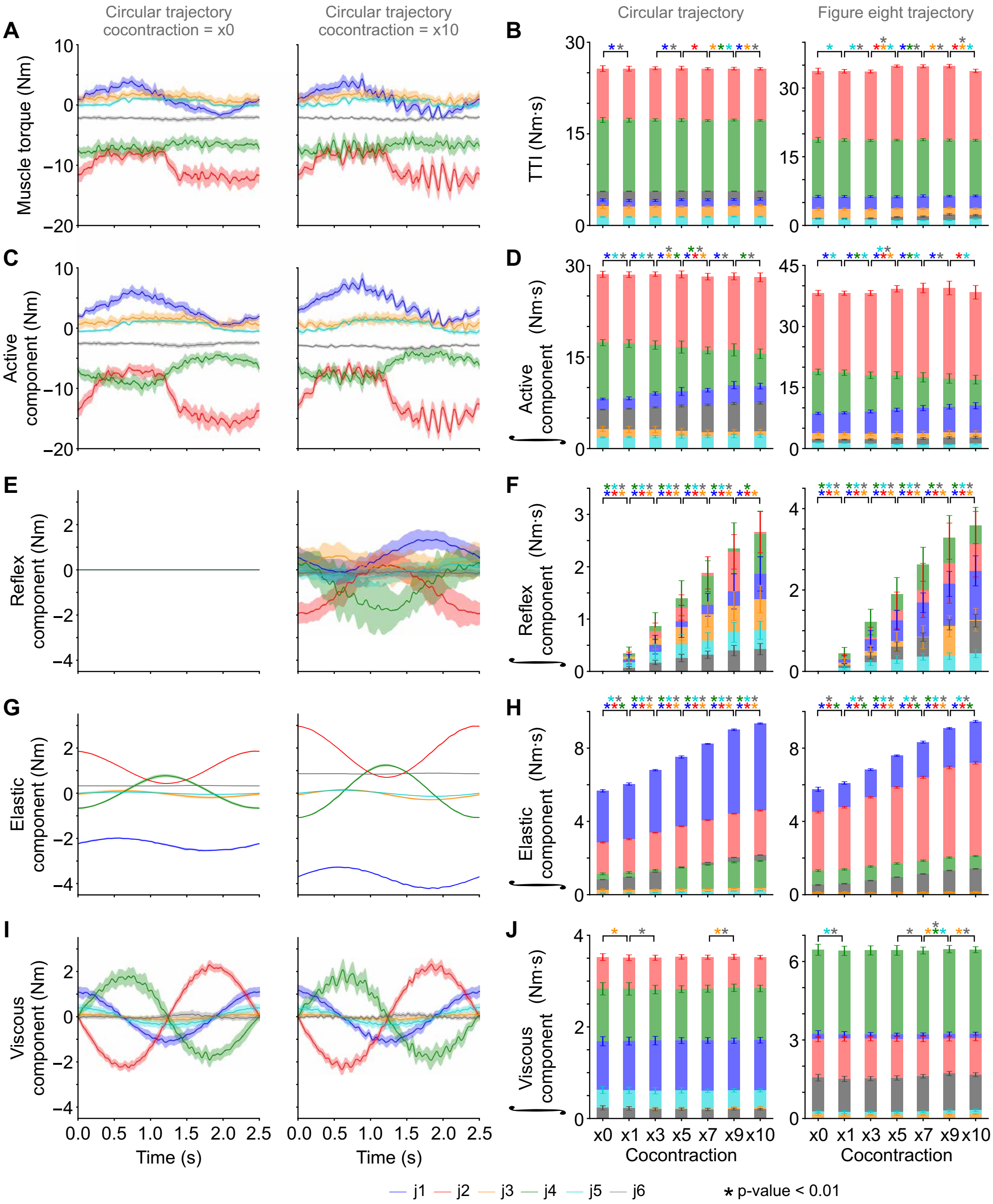

Fig. 4. Muscle torque components. (**A**) Muscle torque profiles of the cerebello-muscular controller performing the circular trajectory with the lowest and highest cocontraction values. (**B**) TTI per joint, across different cocontraction values, performing the circular and figure-eight trajectories. The following muscle torque components are shown, together with their time-integral measurements: (**C**) active component at the lowest and highest cocontraction values for the circular trajectory; (**D**) time integral of the active component for each cocontraction value for the circular and figure-eight trajectories; (**E**) reflex component at the lowest and highest cocontraction values for the circular trajectory; (**F**) time integral of the reflex component for each cocontraction value for the circular and figure-eight trajectories; (**G**) passive elastic component at the lowest and highest cocontraction values for the circular trajectory; (**H**) time integral of the passive elastic component for each cocontraction value for the circular and figure-eight trajectories; (**I**) passive viscous component at the lowest and highest cocontraction values for the circular trajectory; and (**J**) time integral of the passive viscous component for each cocontraction value for the circular and figure-eight trajectories. Data in (A), (C), (E), (G), and (I) show the mean, and shading shows the SD per time step along the trajectory duration using the last 100 trials of the motor adaptation process ($n = 100$). Data in (B), (D), (F), (H), and (J) show the mean, and error bars show the SD per trial using the last 100 trials of the motor adaptation process ($n = 100$). Consecutive cocontraction values were compared using Welch's t test.

the ratio between the applied force (the mass of the attached payload times the gravitational acceleration) and the corresponding deformation (the vertical displacement of the end-effector produced by the attached payload). Differences in the robot arm configuration when performing each trajectory (especially at the position of joint j6) led to differences in the limb stiffness for each trajectory. Nonetheless, a direct relation between cocontraction and limb stiffness was found in both cases (see table S8 for the limb stiffness results).

Downloaded from https://www.science.org at The Hong Kong University of Science and Technology (Guangzhou) on May 25, 2026

To better contextualize the cerebellar control of the muscle-robot dynamics and the behavioral spectrum enabled by our cerebello-muscular controller across the cocontraction range (that is, the degree of motor variability achieved), we tested the response to the payload of a proportional-derivative (PD) controller governing the muscle dynamics under each cocontraction value (Fig. 5A and fig. S4A). The differences between low and high cocontraction values were less pronounced with PD control than with cerebellar control, thereby indicating a narrower range of enabled robot behavior. For the circular trajectory, the cerebellar control of the muscle dynamics allowed a 15.6 times larger range of payload reactions than the PD control: From cocontraction *x0* to *x10*, the cerebellar control showed a deviation range from 0.099 to 0.021 radian (rad), and the PD control ranged from 0.014 to 0.009 rad. Similarly, for the figure-eight trajectory, the cerebello-muscular controller showed a payload reaction range 29 times larger than that of the PD control: From cocontraction *x0* to *x10*, the cerebellar control case allowed a deviation range from 0.069 to 0.011 rad, and the PD control ranged from 0.006 to 0.004 rad (figs. S4B and S5B).

To further deepen the analysis of the behavioral spectrum allowed by our cerebello-muscular controller, we defined a motor behavior metric on the basis of the trajectory deviation induced by the payload. In an HRI environment, physical interactions are determined by the reactions of both agents: the human and the robot. When the physical intentions of the agents are in conflict, the stronger intention will prevail. The more robust agent will dominate the interaction, thus indicating higher "physical agency." Conversely the softer agent will allow a greater deviation from its path, indicating lower physical agency. To quantify this concept, we defined a robot physical agency (RPA) metric on the basis of the trajectory deviation resulting from the applied perturbations. The maximum deviation in position MAE observed for each trajectory (0.099 rad for the circular trajectory and 0.069 rad for the figure-eight trajectory; both allowed by the cerebello-muscular controller with cocontraction *x0*) constituted our RPA value of 0.0 and represented the softest reaction to the perturbation. Conversely, a hypothetical deviation of 0.0 rad represented our maximum RPA value of 1.0, namely, the most robust reaction to the perturbation. The MAE deviation associated with each cocontraction value resulted in an RPA value normalized within this range (see Materials and Methods). Results revealed that the cerebello-muscular controller enabled the robot to exhibit low and high RPA behaviors (both soft and robust reactions), whereas the PD controlling the muscle dynamics only enabled the robot to exhibit high RPA behaviors (Fig. 5B and fig. S4C). In addition, note that the already narrow behavior range provided by the PD would be further restricted if the PD were to be tuned with higher gains to improve accuracy. We observed an inverse relationship between PD gains and the payload reaction range; higher PD gains resulted in a narrowed spectrum of enabled motor behavior (fig. S5). We also tested direct PD control without muscle dynamics, which also demonstrated an inverse relationship between PD gains and payload-induced deviation. Even with low PD gains, which resulted in a significant reduction in accuracy, a soft and compliant behavior was not achieved. Therefore, similar to PD-muscular control, direct PD control did not provide the motor behavior versatility enabled by our cerebello-muscular controller (fig. S5). To visualize the different robot motor behaviors allowed by the cocontraction range, see movie S1.

Downloaded from https://www.science.org at The Hong Kong University of Science and Technology (Guangzhou) on May 25, 2026

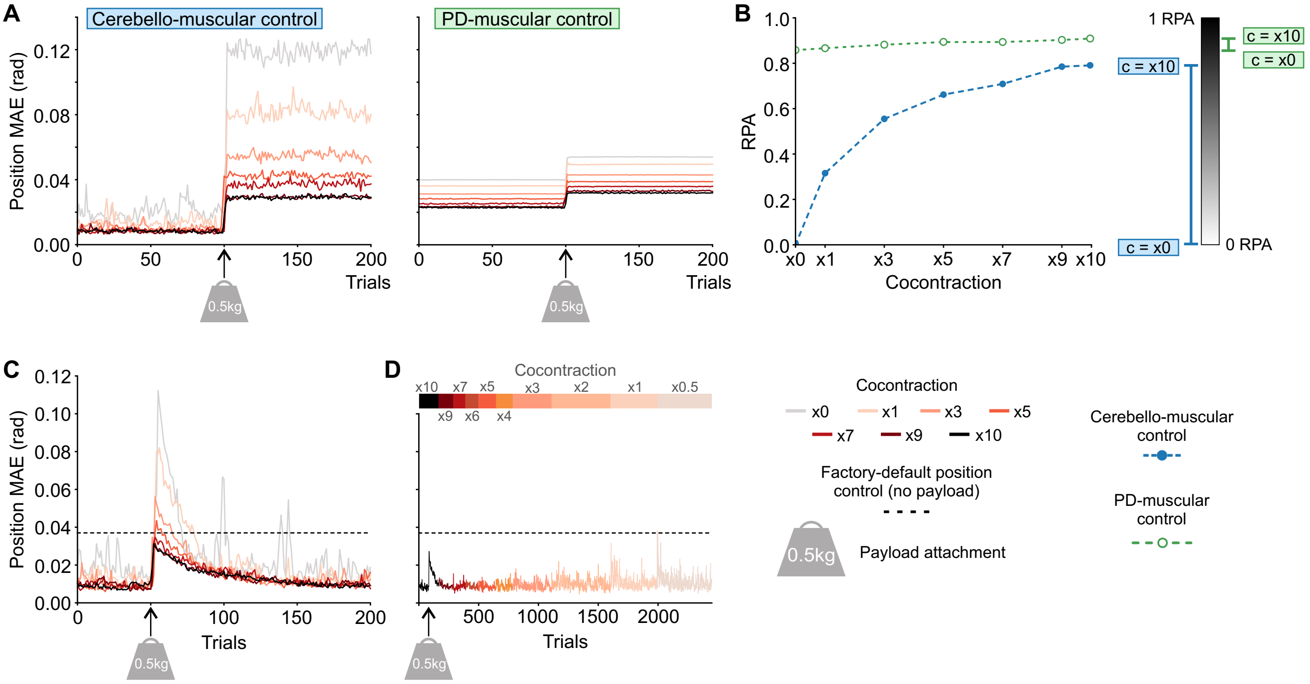

Fig. 5. Cocontraction and response against external perturbations. (**A**) Position MAE before and after attachment of a 0.5-kg payload for the cerebello-muscular controller and PD-muscular controller at varying cocontraction values performing the 2.5-s circular trajectory. (**B**) Spectrum of robot behavior allowed by the cerebello-muscular and PD-muscular controllers, quantified as the RPA. Dashed lines were included as guides to the eye. (**C**) Position MAE evolution during the motor adaptation process of the cerebello-muscular controller after attaching the 0.5-kg payload while performing the circular trajectory. (**D**) Gradual reduction in the cocontraction level after attaching the 0.5-kg payload while performing the circular trajectory.

We then activated cerebellar synaptic plasticity to enable the cerebellum to adapt to the attached payload. Again, higher cocontraction values consistently produced a more robust response, resulting in smaller deviations from the target trajectory. After the initial response to the external payload perturbation, cerebellar adaptation progressed effectively, showing a convergent behavior and allowing successful performance of the motor task despite the presence of the payload for all cocontraction values (Fig. 5C and fig. S4D).

Last, we verified a known biological motor behavior: reacting with high cocontraction as the initial response to unknown dynamics, followed by a gradual decrease in cocontraction as learning and adaptation progressed (*68*–*70*). In our experimental setup, the robot initially performed the motor task with high cocontraction values when the payload was attached. As the cerebellum adapted to the modified dynamics, we were able to gradually decrease cocontraction (Fig. 5D and fig. S4E).

Motor adaptation to low cocontraction enables a seamless transition to higher cocontraction levels

Biological motor learning begins with high muscle cocontraction to minimize initial errors, and it is followed by a gradual decrease in cocontraction levels as learning progresses (*68*). In the early stages of learning, motion is confined to high cocontraction levels because low-cocontraction motor control skills have not yet been acquired; as learning advances, cocontraction can be reduced, and hence the metabolic cost of motion diminishes. This implies that, by the time low cocontraction motion becomes part of the motor repertoire, high cocontraction has previously been mastered, and a seamless transition between cocontraction levels is facilitated. We validated this biological behavior in our robotic setup by applying the learned cerebellar solution developed for a specific cocontraction value to control the muscle dynamics corresponding to other cocontraction values, for both the circular (Fig. 6) and figure-eight (fig. S6) trajectories.

We first applied the cerebellar solution developed for controlling the muscle dynamics at the lowest cocontraction value (*x0*) to control the muscle dynamics for higher cocontraction values. Cerebellar learning was disabled, and the performance started with cocontraction value *x0*; after 50 trials, cocontraction was modified, thus illustrating the continuity of the cerebellar solution. Results showed that mastering the control of the muscle dynamics for cocontraction *x0* enabled successful control of all higher cocontraction values (Fig. 6A and fig. S6A). Subsequently, we applied the cerebellar solution developed for controlling the muscle dynamics at an intermediate cocontraction value (*x5*) to control the muscle dynamics for both lower and higher cocontraction values. After 50 trials performed with cocontraction *x5,* the cocontraction value was modified. Results showed that the cerebellar solution provided precise motor control for higher cocontraction values, but performance declined for lower cocontraction values. Because performance at cocontraction *x1* substantially deteriorated, providing a compelling result, the cerebellar solution acquired for cocontraction *x5* was not further applied to control cocontraction *x0*, hence prioritizing the integrity of the robot (Fig. 6B and fig. S6B). Last, applying the cerebellar solution developed for controlling the muscle dynamics at the highest cocontraction value (*x10*) to all lower cocontraction values revealed precise motor control for cocontraction values *x9* and *x7* (again, the first 50 trials were performed with cocontraction *x10*, and then cocontraction was modified). However, for cocontraction *x5* and *x3*, the tracking error substantially increased. Again, to prioritize the integrity of the robot, the cerebellar solution acquired for cocontraction level *x10* was not further tested to control cocontraction levels *x1* and *x0* for the circular trajectory and *x0* for the figure-eight trajectory (Fig. 6C and fig. S6C).

To understand why cerebellar solutions learned at low cocontraction were effective at higher cocontraction levels but the opposite did not hold, we measured the differences between the learning of these low and high cocontraction cerebellar solutions. After cerebellar motor adaptation to each cocontraction value, we evaluated the complexity of the neural solution at the granule cell–Purkinje cell (GC-PC) neural layer—the only cerebellar layer endowed with synaptic plasticity. This assessment involved computing the entropy of the synaptic weight distribution at the GC-PC layer, providing a value that represents the degree of complexity of the acquired cerebellar solution (see Materials and Methods). The synaptic entropy measurements exhibited a decreasing pattern as cocontraction increased (Fig. 6D and fig. S6D) and showed a high correlation with the position MAE tracking provided by the corresponding cocontraction value. When considering only the synaptic entropy measurements corresponding to cocontraction values that significantly reduced the tracking error (statistical significance shown in Fig. 2, G and H), the entropy measurements followed a linear regression with negative slope (Fig. 6E and fig. S6E). This implies that the higher the cocontraction is, the less complex the required cerebellar solution, suggesting that cocontraction simplified cerebellar motor learning.

Active modulation of cocontraction across different terrains

The results presented so far used externally provided cocontraction, homogeneous to all joints. However, to enable a continuous spectrum ranging from soft to robust motor behavior, active modulation of muscle cocontraction is required. Hence, we developed a strategy to dynamically adjust cocontraction depending on the environment and task requirements on the basis of a weighted trade-off between compliance (soft behavior) and accuracy (robust behavior).

To actively modulate cocontraction, a seamless transition between cocontraction levels must be guaranteed. As observed in the previous section, cerebellar adaptation to low cocontraction enables a seamless transition to higher cocontraction levels; this finding provides the foundation for our cocontraction adjustment strategy. Initially, cerebellar adaptation was set to operate with cocontraction *x0*, thus mimicking the biologically natural motion with low cocontraction in free space (*68*, *69*) and enabling the motor repertoire to effectively range from low to high cocontraction. Then, for a given motor task, priority toward compliant or robust behavior was specified. If compliance was prioritized, cocontraction *x0* was maintained regardless of interactions or perturbations. Conversely, if robustness was prioritized, the cocontraction level increased in response to deviations from the desired trajectory; the stronger the perturbation was, the greater the increase in cocontraction. The priority between compliance and robustness was weighted as $W_{\text{C-R}} \in [0.0, 1.0]$, which could range within the full spectrum from $W_{\text{C-R}} = 0.0$, to establish full compliance priority, to $W_{\text{C-R}} = 1.0$, to establish full robustness priority. The weighted trade-off and the cocontraction level were joint specific, thus allowing for the specific adjustment of the softness/robustness of each joint (see Materials and Methods).

To test active modulation of cocontraction, we expanded the motor benchmark by making the robot perform in different terrains. We designed a T-shaped trajectory (see fig. S1 for the trajectory

Downloaded from https://www.science.org at The Hong Kong University of Science and Technology (Guangzhou) on May 25, 2026

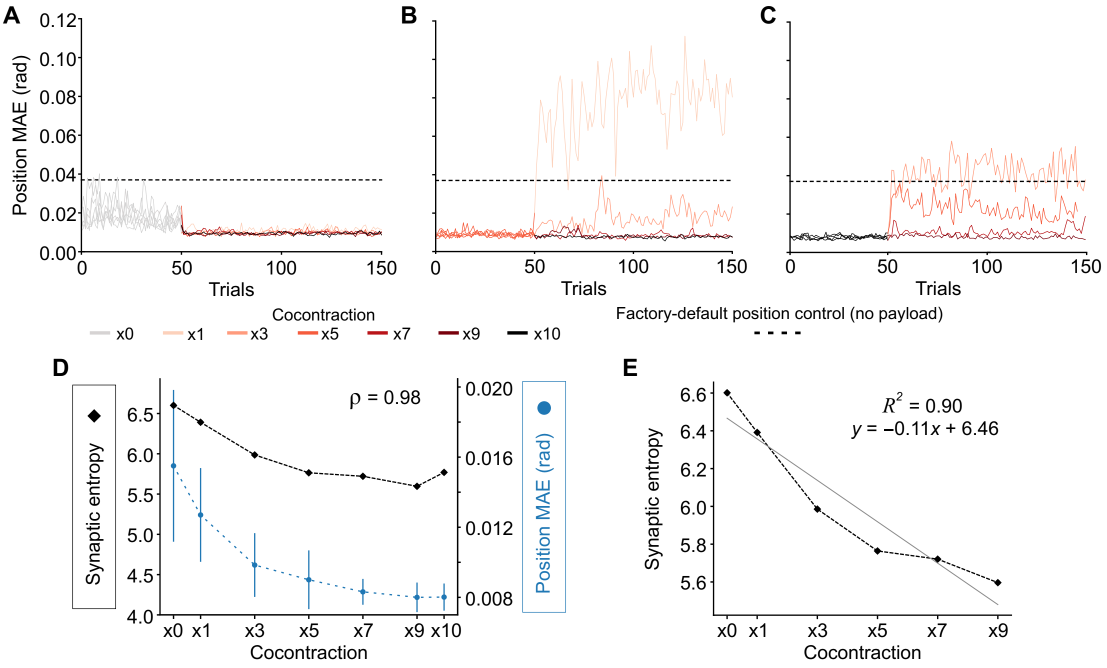

Fig. 6. Application of the cerebellar solution learned for a specific cocontraction value to other cocontraction values while performing the circular trajectory. (**A**) Application of the cerebellar solution learned for cocontraction *x0* to higher cocontraction values. From trial 0 to 50, the cerebello-muscular controller performed with *c* = *x0*, and then the cocontraction value was modified. (**B**) Application of the cerebellar solution learned for cocontraction *x5* to both lower and higher cocontraction values (excluding *c* = *x0* for safety reasons). From trial 0 to 50, the cerebello-muscular controller performed with *c* = *x5*, and then the cocontraction value was modified. (**C**) Application of the cerebellar solution learned for cocontraction *x10* to lower cocontraction values (excluding *c* = *x1* and *c* = *x0* for safety reasons). From trial 0 to 50, the cerebello-muscular controller performed with *c* = *x10*, and then the cocontraction value was modified. In (A) to (C), cerebellar learning was disabled. (**D**) Entropy of the cerebellar (GC-PC) synaptic weights distribution (shown in black) after motor adaptation for each cocontraction value, correlated with the corresponding position MAE (shown in blue). MAE data (taken from Fig. 2G) show the mean, and error bars show the SD of the last 100 trials of the motor adaptation process (*n* = 100). (**E**) Linear regression of synaptic entropy measurements for those cocontraction values that showed a significant improvement in position MAE (statistical significance of position MAE taken from Fig. 2G). Dashed lines in (D) and (E) were included as guides to the eye.

description) to which the cerebellum adapted by operating in free space with cocontraction *x0*. Then, while performing the trajectory, we submerged the robot end effector in fluids of different viscosity (η), consisting of aqueous solutions of xanthan gum (XG) at different concentrations. Specifically, we used 25 liters of water and XG in concentrations of 1, 2, 3, 4, 5, and 6% (see the Supplementary Materials for the viscosity values of the different XG concentrations). The properties of XG allowed us to modify the viscosity of the fluid (*71*); the higher the viscosity was, the greater the constraint for the end-effector motion while submerged in the fluid. For each terrain, we conducted tests with the robot in compliance priority mode ($W_{\text{C-R}} =$ 0.0) and robustness priority mode ($W_{\text{C-R}} = 1.0$) (Fig. 7, A to D, and fig. S7). When compliance was prioritized, the cocontraction level was maintained at *x0* as the end effector was submerged in the fluid (Fig. 7C), resulting in the robot avoiding strong reactions to the perturbations, limiting the end-effector motion, and increasing the overall trajectory deviation (Fig. 7D). Conversely, when robustness was prioritized, the cocontraction level increased as the end effector was submerged in the fluid, resulting in higher cocontraction levels corresponding to increased fluid viscosity (Fig. 7C). The robustness enabled by the increased cocontraction allowed the end effector to cover a wider range of the trajectory despite the fluid viscosity, resulting in a reduced overall trajectory deviation (Fig. 7D). To visualize cocontraction active modulation across different terrains, see movie S2. To focus on the contribution of cocontraction to adapt the motor behavior to different terrains, we disabled cerebellar adaptation in these experiments. With cerebellar adaptation enabled, the cerebellum would gradually absorb the cocontraction contribution, resulting in a progressive reduction in the cocontraction level and error convergence to lower values (fig. S8).

Last, we tested the differentiation of compliant and robust behavior depending on the direction of motion. This was allowed by joint-specific cocontraction; perturbations in one direction were allowed by maintaining low cocontraction in specific joints, whereas perturbations in another direction were rejected by triggering a cocontraction increase in other joints. We differentiated between frontal and lateral motion of the end effector. The T-shaped trajectory and the robot arm configuration determined that frontal motion resulted from the action of joints j2, j4, and j6 and that lateral motion resulted from the action of joint j1. For each terrain, we tested two behavior configurations (Fig. 7, E to G, and fig. S9): frontal robustness and lateral compliance ($W_{\text{C-R}} = 1.0$ for robust behavior at joints j2, j4, and j6, and $W_{\text{C-R}} = 0.0$ for compliant behavior at joint j1) and frontal compliance and lateral robustness ($W_{\text{C-R}} = 0.0$ for compliant behavior at joints j2, j4, and j6, and $W_{\text{C-R}} = 1.0$ for robust behavior at joint j1). In both cases, joints j3 and j5 were set to robust behavior. In the first configuration, the robustness of joints j2, j4, and j6 allowed the end effector to cover a larger distance in the frontal direction, and lateral motion was more constrained. In the second configuration, the robustness of joint j1 allowed the end effector to

Downloaded from https://www.science.org at The Hong Kong University of Science and Technology (Guangzhou) on May 25, 2026

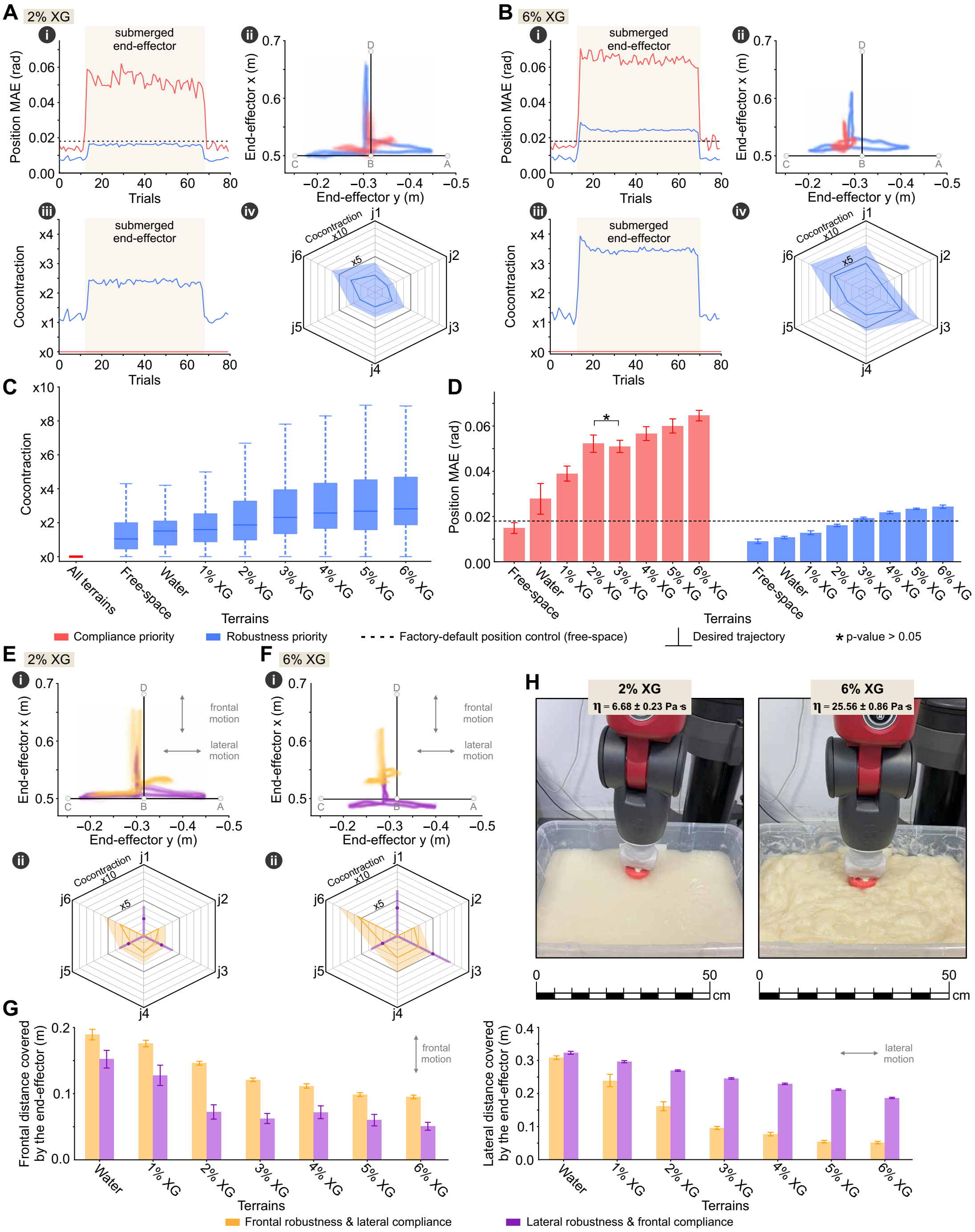

Fig. 7. Active modulation of cocontraction across unknown terrains. (**A**) Compliance priority and robustness priority modes performing in 2% XG and (**B**) 6% XG. (i) Position MAE as the robot end effector is submerged in the viscous fluid. (ii) Cartesian path described by the submerged end effector (density of 50 trials shown). The T-shaped trajectory follows the point sequence A, B, C, B, D, B, A. (iii) Mean cocontraction per trial as the end effector is submerged in the viscous fluid. (iv) Joint cocontraction per trial with submerged end effector (line shows the mean, and shading shows the SD during the first 50 s, sampling every 2 ms). (**C**) Joint cocontraction across terrains in compliance priority and robustness priority modes. Data correspond to the first 50 s with the end effector submerged, sampling every 2 ms (cocontraction from all joints is considered). Boxplots cover from the first to the third quartile, with a line drawn at the median; whiskers extend from the box limits to the farthest data point within 1.5 times the IQR. (**D**) Position MAE in compliance priority and robustness priority modes across all terrains. Data show the mean, and error bars show the SD of 50 trials ($n = 50$) with the end effector submerged. (**E**) Differentiated motor behaviors depending on the direction of motion in 2% XG and (**F**) 6% XG. (i) Cartesian path described by the submerged end effector (density of 50 trials shown). (ii) Joint cocontraction per trial with the end effector submerged (line shows the mean, and shading shows the SD during the first 50 s, sampling every 2 ms). Two motor behaviors were differentiated: frontal robustness and lateral compliance; lateral robustness and frontal compliance. (**G**) Distance covered by the end effector in the frontal and lateral directions across terrains for both motor behaviors. Data show the mean, and error bars show the SD of distance covered per trial by the submerged end effector ($n = 50$ trials). (**H**) End effector submerged in 2% XG and 6% XG.

Downloaded from https://www.science.org at The Hong Kong University of Science and Technology (Guangzhou) on May 25, 2026

cover a larger distance in the lateral direction, and frontal motion was more constrained (Fig. 7G).

DISCUSSION

Robots operating in unstructured scenarios face time-changing physical interactions with the environment, other robots, and/or humans (physical HRI). Fine interactions with the physical world require adjustable robot motor behavior to ensure stability; a trade-off between performance and safety requirements must be reached (*72*). For instance, contact with an unknown surface requires the robot to adjust its stiffness to maintain stability. Similarly, interactions with another agent, such as during a handover, require the robot to adapt to the other's actions and consequences. During physical HRI, low robot stiffness facilitates the human to freely drive the robot; high stiffness is beneficial when the robot is demanded to perform with high accuracy in free space or a soft, controlled environment. Such an adaptive motor behavior has been mastered in nature through the combination of the CNS and body biomechanics (*12*), providing the right balance between precision and flexibility for fine interactions. Biological motor behavior must be understood from a neuromechanics integrative view that can lead to advanced control solutions for robotics (*73*). Within this integrative scope, we mimicked this evolutionary solution by combining a cerebellar SNN with synaptic plasticity and a muscle model that includes an SC-reflex mechanism, cocontraction, and mechanical viscoelasticity. This integration built our cerebello-muscular torque controller, enabling adjustable robot behavior to meet task requirements: regulation of performance accuracy and robustness/softness to external perturbations. The muscle model tunable cocontraction allowed modification of the muscle dynamics, consequently changing the robot stiffness and adjusting its motor behavior. The cerebellar SNN provided the required motor adaptation to command the muscles and drive the robot toward its motor goal despite dynamic changes. We validated the cerebello-muscular torque controller through a motor control benchmark comprising various trajectories at different speeds, external perturbations, and operation across unknown terrains.

The CNS can facilitate movement accuracy by increasing muscle cocontraction, as demonstrated by previous studies wherein cocontraction reduced trajectory variability and tracking error in human arm goal-directed movements (*28*–*30*). In our robotic setup, the increase in cocontraction reduced the trajectory variability and tracking error, thus validating the application of muscle cocontraction to enhance robot performance accuracy. However, there is a limit to this improvement of performance accuracy: There exists a finite range beyond which increasing cocontraction does not improve performance accuracy. The effective cocontraction range depends on the nature of the movement (trajectory and speed of motion); cocontraction requires proper modulation rather than reckless increase.

Another feature of biological cocontraction is that it strengthens joint stiffness (*29*, *30*). It is a means to modulate the mechanical impedance of the body and adjust motor behavior to the environment (*38*), facilitating dynamic stability (*74*) and calibrating the kinematic deviations induced by external perturbations given that higher cocontraction allows smaller deviations under external forces (*61*). In robotics, this adjustable behavior is addressed by variable impedance control. Research efforts have been devoted to varying the robot impedance during task execution and enabling operation across unknown environments. However, the proposed solutions usually face the following limitations (*42*): Traditional variable impedance control relies on accurate dynamic models, which are often nontrivial; unknown environment properties can be compensated for using complex sensing capabilities but at the cost of reducing generalization of these solutions to diverse robots; and learning-based strategies can circumvent the need for analytical modeling but usually depend on specific cost functions and policies for each desired motor behavior.

Apart from variable impedance control, other approaches address a continuous spectrum of motor behavior. That is the case of unified admittance-impedance control, in which the causality of the controller varies depending on the circumstances: Impedance causality (motion inputs and force outputs) is generally better suited for interactions with stiff environments, and admittance causality (force inputs and motion outputs) is better suited for interactions with soft environments (*40*, *75*, *76*). Analytical constraints have usually limited the proposed solutions, and future work is expected to expand these approaches to nonlinear, coupled, multi-DOF robots (*75*–*77*). Here, we adopt impedance causality from a neuromechanics perspective and experimentally validate our cerebello-muscular torque controller using a six-DOF robot with nonlinear joint dynamics.

The original impedance control method already proposed biological muscle redundancies as a solution to modulate mechanical impedance without requiring feedback (*40*). To modulate physical interactions, humans regulate limb stiffness to reduce the dependency on reliable feedback (*45*). Following that approach, we used muscle cocontraction to regulate the robot stiffness and enable a continuous spectrum of adjustable robot motor behavior: Low and high cocontraction allowed for soft and robust behavior against external perturbations, respectively. In addition, by including the cerebellar SNN, we could also address the nonideal effects of nonlinear dynamics and communication delays, a challenge for the unified admittance-impedance control (*78*), which cerebellar SNN robot control inherently copes with (*9*, *10*). Our neuromechanics approach presents a model-free solution, in which impedance is adjusted through muscle activity and integrated as part of the whole system dynamics; cerebellar adaptation acquires the robot and muscle dynamics as a whole. Our control approach does not require separate control laws for robot dynamics and desired impedance, unlike other solutions that implement individual control laws for each (*79*).

Our cerebello-muscular torque controller improved performance accuracy and modulated the motor behavior through subtle changes in the output commands, and it demonstrated a suitable complementarity between the cerebellar slower motor control and the muscular faster motor behavior. Thus, our controller draws another parallel with biological motor control, in which the mechanical properties of muscles and cocontraction allow for inducing substantial changes in behavior by small shifts in the motor commands arising from neural circuitry (*12*).

Studying the synaptic weight distributions of the cerebellar learned solutions elucidated the cocontraction effects on cerebellar learning. Results showed that the higher the cocontraction was, the lower the entropy of the cerebellar GC-PC synaptic weight distribution; high cocontraction levels led to simpler learning computational requirements. This finding is aligned with biological evidence that demonstrates that cocontraction facilitates acquisition of internal models and that it is observed in early stages of learning and then gradually reduced as learning progresses and stabilizes (*68*, *70*). In a previous study, we showed that the SC facilitates cerebellar motor learning (*56*), echoed in

Downloaded from https://www.science.org at The Hong Kong University of Science and Technology (Guangzhou) on May 25, 2026

the present work where the cocontraction increase implied higher SC contribution through stretch reflex. The cerebellar solution acquired for a given cocontraction level could be effectively applied to control the robot under higher cocontraction levels. Thus, motor adaptation to low cocontraction allowed our cerebello-muscular torque controller to seamlessly transition to higher cocontraction levels. This transition enabled a continuous spectrum of robot motor behavior, with soft and robust motor behaviors at opposing ends of the spectrum. This finding also implied a reduction in the operation time required for training: Motor learning can be conducted at low cocontraction, which will also allow performance at high cocontraction without requiring specific training. This is a desirable feature for learning-based methods, which can compensate for inaccurate modeling but usually at the cost of extensive training and data inefficiency (*42*) and typically relying on specific cost functions to achieve different motor behaviors (*80*).

Furthermore, the seamless transition between cocontraction levels enabled the active modulation of cocontraction depending on the terrain and task requirements. Following natural biological motor behavior (low cocontraction motion in free space and cocontraction increase to counteract perturbations), our neuromechanics approach modulates cocontraction to adapt the robot behavior to unknown terrains; the greater the motion constraint imposed by the terrain was, the higher the cocontraction increase and subsequent robot stiffness. In addition, our cocontraction adjustment strategy strictly adhered to the definition of impedance itself (acceptance of motion inputs and response as force outputs) and relied solely on position feedback. This contrasts with variable impedance solutions that rely on contact force sensing capabilities or prior knowledge of the environment characteristics (*79*, *81*). Other variable impedance solutions mimic human stiffness regulation through more complex and specific hardware, such as leader-follower motion-tracking systems or electromyography sensors (*82*, *83*). Our solution directly equips the robot with muscle dynamics to mimic the human behavior, thus rendering robot control independent of external operation or devices. The implemented strategy allowed for a continuous spectrum of robot motor behavior with low technical requirements, simplifying its implementation and application to other robots.

Last, cocontraction modulation was joint specific, enabling more versatile motor behaviors. We differentiated motor behaviors depending on the direction of motion, allowing the robot to reject or accept perturbations depending on their direction. Such a targeted, specific behavior is one of the goals of impedance control (*41*). An ideal impedance controller shall provide the accuracy and robustness of well-designed controllers, along with the flexibility and generalization capabilities of learning-based controllers (*42*). Our neuromechanics approach combines cerebellar adaptability and muscle dynamics to provide a model-free solution for adjustable accuracy, generalization across a continuous spectrum from soft to robust motor behavior, and operation in unknown environments.

Muscle actuation not only poses some challenges for motor control (nonlinearities and higher dimensionality of the control signals) but also presents many benefits (self-stability, computational load reduction, and stiffness modulation through cocontraction) (*22*–*24*, *26*, *27*), and it has inspired hardware-based solutions for robot control (*32*–*34*). Here, we have enlarged the family of muscle-inspired solutions by integrating a software-based muscle model and a cerebellar SNN, which tackles the challenges and harnesses the benefits of muscle-like actuation. The robot was driven through torque commands; however, the deployment of our solution might as well be feasible using other approaches such as torque estimation from current sensing. Further improvement of the model could also be achieved by incorporating more intricate SC circuits that have been shown to facilitate cerebellar learning (*56*) beyond the SC-based reflex presented in the current model.

Our benchmark demonstrated the core features of our neuromechanics approach, with potential applications in physical HRI scenarios. For example, rehabilitation assistance robots should provide motor guidance and movement resistance tailored to the patient's recovery needs (*84*). During initial recovery stages, the robot could prioritize accuracy to assume higher motor responsibilities and guide the patient's movement and then shift to compliance priority to promote the patient to lead the motion as recovery progresses. For movement resistance, the robot stiffness could be adjusted depending on the therapy demands. In addition, feedback from the neuromechanics controller could inform the therapist about the patient's progress. Another example is household robots that must prioritize human safety when interactions occur (*85*) but, at the same time, be able to perform tasks that require accuracy and/or varying stiffness, for instance, different stiffnesses for cleaning or polishing different surfaces. Beyond HRI, neuromechanics approaches could also facilitate locomotion across unstructured terrains; adjustable stiffness is key for successful animal locomotion across various terrains (*86*). The easy implementation of our approach could allow robots to directly benefit from this biological feature and enable stable locomotion in varying environments (*87*, *88*).

Our work embraces previous studies that have elucidated CNS operation and musculoskeletal biomechanics. Continued progress in neuromechanics research will keep pushing forward the development of more advanced robots.

MATERIALS AND METHODS

Objective and study design

We explored the applicability to robotics of a fundamental feature of biological motor control: variable muscle cocontraction to adjust motor behavior in terms of performance accuracy and compliance. To that end, we merged a cerebellar SNN model equipped with synaptic plasticity, a muscle model incorporating both active and passive muscular properties, and a torque-controlled six-DOF robot (Baxter). The combination of these three components constituted our cerebello-muscular robot control loop. The integration used the Robot Operating System (ROS), which facilitated modularity (*89*). The following sections provide further details on the specifics of these elements.

The muscle model

The muscle model was derived from Ekeberg's original muscle implementation, which modeled the mechanical forces induced by the muscles of swimming fish (*46*) and was later adapted to robot control for undulatory swimming research (*48*). These previous implementations modeled an antagonistic muscle pair (the model comprised a flexor and an extensor muscle) and accounted for the viscoelastic properties of muscles, approximated as linear spring dampers. We extended Ekeberg's model to introduce an adjustable cocontraction term and an SC-based reflex component. In our muscle model, the resulting output torque (τ) was given by the following:

Downloaded from https://www.science.org at The Hong Kong University of Science and Technology (Guangzhou) on May 25, 2026

$$\begin{aligned}\tau_j(t) = {} & \alpha_j\left(A_{\mathrm{F},j}(t)-A_{\mathrm{E},j}(t)\right) \\ & + R_{\mathrm{SC},j}(t)+\beta_j\left(A_{\mathrm{F},j}(t)+A_{\mathrm{E},j}(t)+2c_j(t)+\gamma_j\right) \\ & \left(\theta_{\mathrm{r},j}-\theta_{\mathrm{a},j}(t)\right)+\delta_j\theta'_{\mathrm{a},j}(t)\end{aligned} \tag{1}$$

$$R_{\mathrm{SC},j}(t)=\begin{cases}\alpha_j c_j(t)\left(\dfrac{\theta_{\mathrm{d},j}(t)-\theta_{\mathrm{a},j}(t)}{\Delta\theta_{\max}}\right) \text{ if } \left(\theta_{\mathrm{d},j}(t)-\theta_{\mathrm{a},j}(t)\right)<\Delta\theta_{\max} \\ \alpha_j c_j(t) \text{ if } \left(\theta_{\mathrm{d},j}(t)-\theta_{\mathrm{a},j}(t)\right)\geq\Delta\theta_{\max}\end{cases} \tag{2}$$

where $j \in [1, 6]$ stands for the joint index; α_j corresponds to the muscle activation gain of each joint; $A_{\mathrm{F},j}$ and $A_{\mathrm{E},j}$ are the cerebellar muscle activation commands for flexion and extension, respectively; $R_{\mathrm{SC},j}$ is the SC-based reflex component; β_j is the muscle stiffness gain; c_j stands for the cocontraction level; γ_j is the muscle tonic stiffness; $\theta_{\mathrm{r},j}$ is the joint resting position; $\theta_{\mathrm{a},j}$ is the joint actual position; δ_j stands for the damping coefficient; $\theta'_{\mathrm{a},j}$ is the joint velocity; and t stands for time (sampling in time steps of 2 ms). Please refer to the Supplementary Materials (table S1) for the values of each muscle parameter. The SC-based reflex component was determined by the cocontraction level (c) and the mismatch between the desired and actual joint positions (θ_{d} and θ_{a}). It was saturated when the mismatch exceeded the maximum allowed deviation ($\Delta\theta_{\max} = 0.35$ rad for all joints). The adjustable cocontraction level established a baseline muscle activation in both flexion and extension direction of movement; A_{F} and A_{E} became ($A_{\mathrm{F}} + c$) and ($A_{\mathrm{E}} + c$). Varying the c values across a wide range adjusted the muscle dynamics, resulting in different motor behaviors.

The output muscle torque (τ) resulted from the combination of the different muscle components (Fig. 4): active component, SC-based reflex component, elastic component, and viscous component. The cerebellum directly controlled the muscle active component by adapting the descending activation commands to drive the movement in either the flexion or extension direction. From Eq. 1, the muscle active component was characterized by

$$\alpha_j\left(A_{\mathrm{F},j}-A_{\mathrm{E},j}\right) \tag{3}$$

The reflex component (R_{SC}), defined in Eq. 2, operated as a spinal stretch reflex on the basis of the equilibrium point (EP) hypothesis (*90*, *91*). The stretch reflex responds to changes in muscle length detected by muscle spindles. In our model, the reflex responded to changes in joint position, which can be derived from muscle length (*92*, *93*). Our EP shifted around the desired position (*62*), thus enabling goal-directed movements and reproducing SC functionality (*92*, *94*). In the EP hypothesis, the CNS specifies the threshold of the spinal stretch reflex (*61*), found to be modulated by descending signals during voluntary movements (*95*–*97*). In our model, the reflex was modulated by the cocontraction level, which has been modeled together with the EP hypothesis to compensate for loads during arm movements (*62*).

The muscle elastic component drove each joint toward its resting position. The arm resting position was defined as the joint configuration at which, once settled, zero torque did not induce any robot motion (see fig. S12 for an illustration of the robot resting position). From Eq. 1, the elastic component was characterized by

$$\beta_j\left(A_{\mathrm{F},j}+A_{\mathrm{E},j}+2c_j+\gamma_j\right)\left(\theta_{\mathrm{r},j}-\theta_{\mathrm{a},j}\right) \tag{4}$$

Last, the viscous component was determined by the joint velocity and the muscle damping coefficient. From Eq. 1, it was characterized by

$$\delta_j\theta'_{\mathrm{a},j} \tag{5}$$

Further analysis of the muscle components is illustrated in fig. S10, highlighting the contribution of each muscle component through ablation experiments. Ablation of the SC-reflex component deteriorates performance accuracy and facilitates output torque convergence because the controller lacks the reflex fast corrective term, which helps improve accuracy but can cause early-stage oscillations. Ablation of the elastic component slightly improves performance accuracy, given that the controller no longer needs to compensate for the elasticity pulling the arm to its resting position. Ablation of the viscous component leads to oscillations and deteriorates performance accuracy because of the lack of damping response.

Active modulation of cocontraction

Active modulation of the cocontraction level was joint specific; it depended on deviations from the desired joint trajectory, and it was based on a weighted trade-off between compliance and accuracy. Cocontraction was dynamically adjusted as follows:

$$c_j(t) = 20\left(W_{\mathrm{C\text{-}R},j}\right)^3 \cdot \frac{\left|\theta_{\mathrm{d},j}(t)-\theta_{\mathrm{a},j}(t)\right|}{e^{-2W_{\mathrm{C\text{-}R},j}}} \tag{6}$$

where $j \in [1, 6]$ stands for the joint index; c_j stands for the joint cocontraction; $W_{\mathrm{C\text{-}R},j} \in [0.0, 1.0]$ stands for the joint compliance-robustness weighted priority, with $W_{\mathrm{C\text{-}R},j} = 0$ defining the compliance priority mode and $W_{\mathrm{C\text{-}R},j} = 1$ defining the robustness priority mode; and $\theta_{\mathrm{d},j}$ and $\theta_{\mathrm{a},j}$ are the desired and actual joint positions, respectively (t stands for time). The resulting cocontraction value was constrained to the range [0.0, 10.0] and then normalized within the range [0.0, 1.0] before entering the muscle model equation (cocontraction ranging from *x0* to *x10*).

The cerebellar model

The cerebellar SNN, built on previous works (*9*, *10*, *56*), is derived from the Marr-Albus-Ito cerebellar theory (*50*–*52*), which established the foundation for supervised motor learning in the cerebellum (*53*). The cerebellar network comprised 16,374 neurons distributed across five neural layers that were divided into six microcomplexes each (*98*). These microcomplexes processed the sensorimotor data related to each of the six DOF of the robot. The intricate cerebellar network orchestrated, via neural adaptation, the translation of sensorimotor information into coordinated muscle activation commands for the robot movement.

The implemented cerebellar neural layers were the following: mossy fibers (MFs), GCs, PCs, climbing fibers (CFs), and deep cerebellar nuclei (DCNs) (refer to the Supplementary Materials for the cerebellar neural network topology). The MFs (168 neurons) encoded the robot sensory information (desired and actual state of the joints) as afferent projections to the cerebellum, which formed excitatory synapses with the GCs. The GCs (14,406 neurons) univocally

Downloaded from https://www.science.org at The Hong Kong University of Science and Technology (Guangzhou) on May 25, 2026

recoded the received sensory input (*99*), which was then transmitted through excitatory connections to the PCs (600 neurons). The PC layer also received excitatory inputs from the CFs (600 neurons), which conveyed an instructive signal per joint that represented the mismatch between the desired and actual joint state. The PC layer, in turn, projected inhibitory connections to the DCN layer (600 neurons), which also received excitatory synapses from MFs and CFs. Last, the DCN activity provided the cerebellar efferent projections, delivering the agonist-antagonist activation commands (A_F and A_E) to the muscle model for flexion-extension control. To differentiate between flexion and extension control, the DCN layer maintained separate agonist-antagonist subpopulations, thus allowing each microcomplex to generate the two output signals for the corresponding joint: The agonist DCN subpopulation generated the flexion activation command (A_F); the antagonist subpopulation generated the extension activation command (A_E).

Cerebellar adaptation was facilitated via a spike timing–dependent plasticity (STDP) mechanism, which correlated input sensory information with the instructive signal and adjusted accordingly the synaptic weights in the GC-PC connections. This STDP mechanism was ruled by the balance between two opposed processes: long-term potentiation (LTP) and long-term depression (LTD). LTP induced a fixed synaptic weight increment for every spike that reached a PC through a GC as follows:

$$\text{LTP } \Delta w_{\text{GC}_j-\text{PC}_i}(t) = \alpha \cdot \delta_{\text{GC}}(t) \cdot dt \tag{7}$$

where $\Delta w_{\text{GC}j\text{-PC}i}$ denotes the synaptic weight change between the *j*th GC and *i*th PC; $\alpha = 0.002$ nS is the synaptic weight increment; and δ_{GC} is the Dirac delta function of a GC spike. The LTD process, which depressed the GC-PC synaptic weights, correlated the GC and CF activity as follows:

$$\text{LTD } \Delta w_{\text{GC}_j-\text{PC}_i}(t) = \beta \cdot \int_{-\infty}^{t_{\text{CF}}} k\left(t - t_{\text{CF}}\right) \cdot \delta_{\text{GC}}(t) \cdot dt \tag{8}$$

$$k(x) = \begin{cases} \dfrac{-\left(x + d_k\right)}{\varphi_{\text{LTD}} - d_k} \cdot e^{\frac{x+d_k}{\varphi_{\text{LTD}}-d_k}+1} & \text{if } x < -d_k \\ 0 & \text{if } x \geq -d_k \end{cases} \tag{9}$$

where $\beta = -0.0008$ nS denotes the synaptic weight decrement; t_{CF} is the arrival time of a CF spike; $k(x)$ defines an integrative kernel, where $d_k = 120$ ms established the kernel width; and $\varphi_{\text{LTD}} = 150$ ms is the kernel eligibility trace peak, which establishes that the synaptic weight decrement is maximum for the GC spikes received φ_{LTD} ms before the arrival of a CF spike [for $x = \varphi_{\text{LTD}}$; $k(x) = 1$]. This interplay between LTP and LTD temporally correlated the instructive signal (CF activity) with the previous sensory state (GC activity).

The regulation of the GC-PC synaptic distribution, in turn, modulated the cerebellar efferent projections; the inhibitory action of PCs on DCN neurons shaped the cerebellar output commands. The cerebellar output commands arose from DCN activity: Each DCN microcomplex generated the joint agonist-antagonist pair of output activation commands (A_F and A_E). These commands were computed from the DCN activity as follows:

$$\text{DCN}_{j,i}(t) = \int_{t-T_{\text{step}}}^{t} \delta_{\text{DCN}j,i}(t) \cdot dt \tag{10}$$

$$\begin{aligned} \text{DCN}_{\text{AG},j}(t) &= \frac{1}{M_j} \cdot \sum_{i=1}^{i=50} \left[\alpha_j \cdot \text{DCN}_{j,i}(t)\right] \\ \text{DCN}_{\text{ANT},j}(t) &= \frac{1}{M_j} \cdot \sum_{i=51}^{i=100} \left[\alpha_j \cdot \text{DCN}_{j,i}(t)\right] \end{aligned} \tag{11}$$

$$\begin{aligned} A_{\text{F},j}(t) &= \frac{1}{21} \cdot \sum_{x=0}^{20} \text{DCN}_{\text{AG},j}\left(t - x \cdot T_{\text{step}}\right) \\ A_{\text{E},j}(t) &= \frac{1}{21} \cdot \sum_{x=0}^{20} \text{DCN}_{\text{ANT},j}\left(t - x \cdot T_{\text{step}}\right) \end{aligned} \tag{12}$$

where $j \in [1, 6]$ stands for the joint index; *i* is the DCN neuron index within the microcomplex, which was halved in agonist ($i \in [1, 50]$) and antagonist subpopulations ($i \in [51, 100]$); T_{step} is the 2-ms duration of a time step; δ_{DCN} is the Dirac delta function of a DCN spike; DCN_{AG} and DCN_{ANT} are the agonist and antagonist outputs of the microcomplex; $\alpha_j = [0.75, 1.0, 0.375, 0.5, 0.05, 0.05]$ defines an output gain to weigh each joint relative position and mass; and $M_j = [15.0, 25.0, 9.0, 12.5, 1.8, 1.0]$ is a normalization factor used to normalize DCN_{AG} and DCN_{ANT} within the range [0, 1] (DCN_{AG} and DCN_{ANT} saturated to 1.0). The DCN agonist and antagonist outputs were then filtered (mean filter of size 21), providing A_F and A_E per joint to command the muscle model.

Please refer to the Supplementary Materials for a comprehensive understanding of the implemented leaky integrate-and-fire neuron model (*100*), the translation process from the robot analog domain to spiking neural activity, and the computation of the cerebellar instructive signal. Further details can also be found in (*9*, *10*, *56*), from which this model was built on.

The robot

We used the Baxter robot (*49*) as the front-end body of our cerebello-muscular control loop. Baxter is a collaborative robot equipped with two arms and series elastic actuators and allows for torque control (*101*). Our benchmark involved six DOFs of Baxter's right arm (fig. S12). Baxter is known for its accuracy limitations, which are further highlighted when working at high speed (*102*, *103*). We used the factory-default position controller as a baseline to define appropriate performance for the robot in use. The factory-default position controller is the position control method provided by the manufacturer. In position control mode, a position command (desired position coordinate for each joint) is directly sent to the robot, which internally handles the application of the desired position through the factory-default position controller. Parameterization of this internal controller is not provided by the manufacturer. For a computational complexity analysis, please refer to the Supplementary Materials.

The motor control benchmark

The motor control benchmark aimed to capture the complex dynamics of the six-DOF robot arm, including nonlinearities and joint interaction forces. We designed a set of sinusoidal-like and bell-shaped joint trajectories (position and velocity coordinates) performed at different speeds (*104*, *105*). This set of trajectories provided three different desired paths for the end effector to follow: a circular trajectory performed in the vertical plane, a figure-eight trajectory performed in the horizontal plane, and a T-shaped trajectory performed in the horizontal plane. Please refer to the Supplementary Materials for detailed descriptions of the joint coordinates

Downloaded from https://www.science.org at The Hong Kong University of Science and Technology (Guangzhou) on May 25, 2026

corresponding to each motor task. To evaluate the response to external perturbations, we attached a 0.5- and 1.0-kg payload to the end effector during the circular and figure-eight trajectories, respectively. To test cocontraction across different terrains and to assess the active modulation of cocontraction, we submerged the end effector in fluids of different viscosity while performing the T-shaped trajectory. The terrains consisted of an aqueous solution of XG at different concentrations. The rheological properties of XG allowed us to cover a wide viscosity range (*71*).

The fluid viscosity was measured using a Haake MARS III controlled-stress rheometer (Thermo Fisher Scientific, Waltham, MA, USA) equipped with a concentric cylinder geometry. For each terrain, three repetitions of the viscosity measurement were taken to ensure the accuracy and reliability of the results (fig. S11 and table S9).

Performance accuracy metric

The performance accuracy was determined by the difference between the desired and actual trajectories. At each time step, we measured the difference between the desired and actual joint positions (θ_d and θ_a) and computed the average difference through the duration of the motor task. The accuracy of a motor task trial, measured as the position MAE, was given by the joint average error as follows:

$$\mathrm{MAE}_j = \frac{T_{\mathrm{step}}}{T} \sum_{t=0\ \mathrm{s}}^{T} \left| \theta_{\mathrm{d},j}(t) - \theta_{\mathrm{a},j}(t) \right| \tag{13}$$

$$\mathrm{MAE} = \frac{1}{N} \sum_{j=1}^{N} \mathrm{MAE}_j \tag{14}$$

where T_{step} is the 2-ms time step, T denotes the motor task duration, $j \in [1, 6]$ is the joint index, and $N = 6$ is the total number of joints. Our final metric was defined by the mean and SD of the position MAE observed over the final 100 trials of the motor adaptation process.

TTI metric

To quantify the amount of joint torque used during the execution of the motor tasks, we calculated the joint TTI (*64–67*) throughout the motor task duration. The TTI for each trial of the motor task was calculated as follows:

$$\mathrm{TTI} = \int_{t=0\ \mathrm{s}}^{T} \tau_j(t) \cdot dt \tag{15}$$

where τ_j defines the joint torque commanded to the robot at each time step. The final TTI metric was determined by the mean and SD over the final 100 trials of the motor adaptation process. This method was also used to compute the time-integral measurements for the different muscle components.

RPA metric

The assessment of RPA was based on the different behaviors resulting from the varying level of cocontraction. These differences were observed through the robot response when attaching a payload to the end effector (0.5 kg for the circular trajectory; 1 kg for the figure-eight trajectory). We measured the difference in robot performance before and after attaching the payload for each cocontraction value. This difference was defined as the payload-induced deviation, Δ_{MAE}, and was calculated as follows:

$$\Delta_{\mathrm{MAE}} = \mathrm{MAE}_{\mathrm{post-payload}} - \mathrm{MAE}_{\mathrm{pre-payload}} \tag{16}$$

where $\mathrm{MAE}_{\text{post-payload}}$ and $\mathrm{MAE}_{\text{pre-payload}}$ were given by the mean position MAE obtained from 100 trials performed with and without the payload, respectively. On the basis of the deviations induced by the payload in each motor task scenario, we defined our RPA metric. A hypothetical deviation of 0.0 rad (Δ_{MAEmin}) would indicate the most robust robot response to the perturbation, thus correlating to the highest RPA = 1.0. Conversely, the greatest deviation (Δ_{MAEmax}) found experimentally within the cocontraction range indicated the softest robot reaction to the perturbation, thus correlating to the lowest RPA = 0.0. We obtained a normalized RPA value from the deviation allowed by each cocontraction value, Δ_{MAE}, as follows:

$$\mathrm{RPA} = 1.0 - \frac{\Delta_{\mathrm{MAE}}}{\Delta_{\mathrm{MAEmax}}} \tag{17}$$

PD control of the muscle dynamics

To contextualize the complementarity of the cerebellum and muscle dynamics and the spectrum of motor behavior enabled by our cerebello-muscular controller, we also tested the muscle dynamics commanded by a PD controller. The implemented muscle dynamics differentiated between flexion and extension activation commands (A_{F} and A_{E}), which could be provided by the cerebellum given the division of the DCN layer into agonist and antagonist zones. Given that a PD controller lacks this division, the muscle model under PD control had to be modified as follows:

$$\begin{aligned} \tau_j(t) = {} & \alpha_j\left(PD_{\mathrm{output},j}(t)\right) + R_{\mathrm{SC},j}(t) \\ & - \beta_j\left(2c(t) + \gamma_j\right)\left(\theta_{\mathrm{r},j} - \theta_{\mathrm{a},j}(t)\right) + \delta_j \theta'_{\mathrm{a},j}(t) \end{aligned} \tag{18}$$

$$PD_{\mathrm{output},j}(t) = k_{\mathrm{p},j}\left(\theta_{\mathrm{d},j}(t) - \theta_{\mathrm{a},j}(t)\right) + k_{\mathrm{d},j}\left(\theta'_{\mathrm{d},j}(t) - \theta'_{\mathrm{a},j}(t)\right) \tag{19}$$

where $k_{\mathrm{p},j}$ and $k_{\mathrm{d},j}$ are the proportional and derivative gain of each joint, respectively, and the rest of the muscle components remain the same as for the cerebello-muscular controller. Please see table S5 for the PD gains for each trajectory. When testing the reaction to the 0.5-kg payload while performing the circular trajectory, we also tested a PD with higher gains governing the muscle dynamics (fig. S5). Please see table S6 for the higher PD gains for the circular trajectory. To further contextualize our solution, we also tested direct PD control without muscle dynamics (fig. S5) using three different PD controllers (v1, v2, and v3) performing the circular trajectory. Please see table S7 for the PD gains of the three different direct PD controllers.

Evaluation of the cerebellar learned solutions

To evaluate the cerebellar learned solutions, we measured the complexity of the GC-PC synaptic weight distribution acquired after motor adaptation for each cocontraction value. The 14,406 GC neurons innervated the 600 PC neurons in an all-to-one manner; each PC received an excitatory synapse from every GC. Therefore, the synaptic weight distribution of the GC-PC layer was represented by a matrix ($W_{\text{GC-PC}}$) of size I x J, with $I = 14{,}406$ and $J = 600$ for

Downloaded from https://www.science.org at The Hong Kong University of Science and Technology (Guangzhou) on May 25, 2026

the total number of GC and PC neurons, respectively. Each cell in the matrix stored the synaptic weight (w) between GC_i and PC_j as follows:

$$W_{\mathrm{GC-PC}} = \begin{bmatrix} w_{1,1} & w_{1,2} & \dots & w_{1,J} \\ w_{2,1} & w_{2,2} & \dots & w_{2,J} \\ \dots & \dots & \dots & \dots \\ w_{I,1} & w_{I,2} & \dots & w_{I,J} \end{bmatrix} \tag{20}$$

Once the synaptic weight distribution matrix for each cocontraction value was obtained, we applied Shannon's entropy using a Python library (*106*). The entropy value provided a quantifiable metric of the complexity found in each GC-PC synaptic weight distribution (*56*). Higher entropy values indicated greater complexity within the obtained cerebellar solution.

Statistical analysis

Statistical significance presented in Figs. 2 (G and H), 3, 4 (B, D, F, H, and J), and 7 (C and D) was obtained by comparing the samples of consecutive cocontraction values using Welch's t test (*107*) implementation in the SciPy open-source software (function scipy.stats.ttest_ind) (*108*). The figures display the P values (*) below the threshold indicated in the figure legend, except for Fig. 7 (C and D), in which the P values greater than the threshold are displayed for visual simplicity of the figure. The boxplots in Fig. 7C cover from the first to the third quartile, with a line drawn at the median (cocontraction from all joints was considered); whiskers extend from the box limits to the farthest data point within 1.5 times the interquartile range (IQR).

Supplementary Materials

The PDF file includes:
Methods
Tables S1 to S9
Figs. S1 to S12
Results
Legends for movies S1 and S2
References (*109*–*114*)

Other Supplementary Material for this manuscript includes the following:
Movies S1 and S2

REFERENCES AND NOTES

1. G.-Z. Yang, J. Bellingham, P. E. Dupont, P. Fischer, L. Floridi, R. Full, N. Jacobstein, V. Kumar, M. McNutt, R. Merrifield, B. J. Nelson, B. Scassellati, M. Taddeo, R. Taylor, M. Veloso, Z. L. Wang, R. Wood, The grand challenges of science robotics. *Sci. Robot.* **3**, eaar7650 (2018).
2. M. Kennedy III, The role of collaborative robotics in assistive and rehabilitation applications. *Sci. Robot.* **8**, eadk6743 (2023).
3. V. Ortenzi, A. Cosgun, T. Pardi, W. P. Chan, E. Croft, D. Kulić, Object handovers: A review for robotics. *IEEE Trans. Robot.* **37**, 1855–1873 (2021).
4. R. Pfeifer, M. Lungarella, F. Iida, Self-organization, embodiment, and biologically inspired robotics. *Science* **318**, 1088–1093 (2007).
5. D. Floreano, A. J. Ijspeert, S. Schaal, Robotics and neuroscience. *Curr. Biol.* **24**, R910–R920 (2014).
6. M. Chahine, R. Hasani, P. Kao, A. Ray, R. Shubert, M. Lechner, A. Amini, D. Rus, Robust flight navigation out of distribution with liquid neural networks. *Sci. Robot.* **8**, eadc8892 (2023).
7. J. Dupeyroux, J. R. Serres, S. Viollet, AntBot: A six-legged walking robot able to home like desert ants in outdoor environments. *Sci. Robot.* **4**, eaau0307 (2019).
8. S. Ma, J. Pei, W. Zhang, G. Wang, D. Feng, F. Yu, C. Song, H. Qu, C. Ma, M. Lu, F. Liu, W. Zhou, Y. Wu, Y. Lin, H. Li, T. Wang, J. Song, X. Liu, G. Li, R. Zhao, L. Shi, Neuromorphic computing chip with spatiotemporal elasticity for multi-intelligent-tasking robots. *Sci. Robot.* **7**, eabk2948 (2022).
9. I. Abadía, F. Naveros, J. A. Garrido, E. Ros, N. R. Luque, On robot compliance: A cerebellar control approach. *IEEE Trans. Cybern.* **51**, 2476–2489 (2019).
10. I. Abadía, F. Naveros, E. Ros, R. R. Carrillo, N. R. Luque, A cerebellar-based solution to the nondeterministic time delay problem in robotic control. *Sci. Robot.* **6**, eabf2756 (2021).
11. R. Pfeifer, J. Bongard, *How the Body Shapes the Way We Think: A New View of Intelligence* (MIT Press, 2006).
12. E. Tytell, P. Holmes, A. H. Cohen, Spikes alone do not behavior make: Why neuroscience needs biomechanics. *Curr. Opin. Neurobiol.* **21**, 816–822 (2011).
13. S. Collins, A. Ruina, R. Tedrake, M. Wisse, Efficient bipedal robots based on passive-dynamic walkers. *Science* **307**, 1082–1085 (2005).
14. A. J. Ijspeert, Biorobotics: Using robots to emulate and investigate agile locomotion. *Science* **346**, 196–203 (2014).
15. S. Wolf, G. Grioli, O. Eiberger, W. Friedl, M. Grebenstein, H. Höppner, E. Burdet, D. G. Caldwell, R. Carloni, M. G. Catalano, D. Lefeber, S. Stramigioli, N. Tsagarakis, M. Van Damme, R. Van Ham, B. Vanderborght, L. C. Visser, A. Bicchi, A. Albu-Schaffer, Variable stiffness actuators: Review on design and components. *IEEE/ASME Trans. Mechatron.* **21**, 2418–2430 (2015).
16. Y. Wang, X. Yang, Y. Chen, D. K. Wainwright, C. P. Kenaley, Z. Gong, Z. Liu, H. Liu, J. Guan, T. Wang, J. C. Weaver, R. J. Wood, L. Wen, A biorobotic adhesive disc for underwater hitchhiking inspired by the remora suckerfish. *Sci. Robot.* **2**, eaan8072 (2017).
17. C. Laschi, B. Mazzolai, M. Cianchetti, Soft robotics: Technologies and systems pushing the boundaries of robot abilities. *Sci. Robot.* **1**, eaah3690 (2016).
18. A. R. Sobinov, S. J. Bensmaia, The neural mechanisms of manual dexterity. *Nat. Rev. Neurosci.* **22**, 741–757 (2021).
19. M. W. Marzke, Upper-limb evolution and development. *J. Bone Joint Surg. Am.* **91**, 26–30 (2009).
20. R. Gopura, K. Kiguchi, E. Horikawa, A study on human upper-limb muscles activities during daily upper-limb motions. *Int. J. Bioelectromagn.* **12**, 54–61 (2010).
21. D. C. Taylor, J. D. Dalton Jr., A. V. Seaber, W. E. Garrett Jr., Viscoelastic properties of muscle-tendon units: The biomechanical effects of stretching. *Am. J. Sports Med.* **18**, 300–309 (1990).
22. H. Wagner, R. Blickhan, Stabilizing function of antagonistic neuromusculoskeletal systems: An analytical investigation. *Biol. Cybern.* **89**, 71–79 (2003).
23. R. Blickhan, A. Seyfarth, H. Geyer, S. Grimmer, H. Wagner, M. Günther, Intelligence by mechanics. *Philos. Trans. R. Soc. London Ser. A Math. Phys. Eng. Sci.* **365**, 199–220 (2007).
24. I. E. Brown, G. E. Loeb, "A reductionist approach to creating and using neuromusculoskeletal models" in *Biomechanics and Neural Control of Posture and Movement*, J. M. Winters, P. E. Crago, Eds. (Springer, 2000), pp. 148–163.
25. H. Hauser, A. J. Ijspeert, R. M. Füchslin, R. Pfeifer, W. Maass, Towards a theoretical foundation for morphological computation with compliant bodies. *Biol. Cybern.* **105**, 355–370 (2011).
26. D. Haeufle, M. Günther, G. Wunner, S. Schmitt, Quantifying control effort of biological and technical movements: An information-entropy-based approach. *Phys. Rev. E* **89**, 012716 (2014).
27. D. F. Haeufle, I. Wochner, D. Holzmüller, D. Driess, M. Günther, S. Schmitt, Muscles reduce neuronal information load: Quantification of control effort in biological vs. robotic pointing and walking. *Front. Robot. AI* **7**, 511258 (2020).
28. P. L. Gribble, L. I. Mullin, N. Cothros, A. Mattar, Role of cocontraction in arm movement accuracy. *J. Neurophysiol.* **89**, 2396–2405 (2003).
29. R. Osu, N. Kamimura, H. Iwasaki, E. Nakano, C. M. Harris, Y. Wada, M. Kawato, Optimal impedance control for task achievement in the presence of signal-dependent noise. *J. Neurophysiol.* **92**, 1199–1215 (2004).
30. L. P. Selen, P. J. Beek, J. H. Van Dieën, Impedance is modulated to meet accuracy demands during goal-directed arm movements. *Exp. Brain Res.* **172**, 129–138 (2006).
31. W. Liang, H. Liu, K. Wang, Z. Qian, L. Ren, L. Ren, Comparative study of robotic artificial actuators and biological muscle. *Adv. Mech. Eng.* **12**, 1687814020933409 (2020).
32. Y. Morimoto, H. Onoe, S. Takeuchi, Biohybrid robot powered by an antagonistic pair of skeletal muscle tissues. *Sci. Robot.* **3**, eaat4440 (2018).
33. X. Ji, X. Liu, V. Cacucciolo, M. Imboden, Y. Civet, A. El Haitami, S. Cantin, Y. Perriard, H. Shea, An autonomous untethered fast soft robotic insect driven by low-voltage dielectric elastomer actuators. *Sci. Robot.* **4**, eaaz6451 (2019).
34. D. Büchler, R. Calandra, J. Peters, Learning to control highly accelerated ballistic movements on muscular robots. *Robot. Auton. Syst.* **159**, 104230 (2023).
35. Y. Mengüç, N. Correll, R. Kramer, J. Paik, Will robots be bodies with brains or brains with bodies? *Sci. Robot.* **2**, eaar4527 (2017).
36. R. Raman, R. Bashir, Biomimicry, biofabrication, and biohybrid systems: The emergence and evolution of biological design. *Adv. Healthc. Mater.* **6**, 1700496 (2017).
37. H. Chaoui, P. Sicard, W. Gueaieb, ANN-based adaptive control of robotic manipulators with friction and joint elasticity. *IEEE Trans. Ind. Electron.* **56**, 3174–3187 (2009).
38. N. Hogan, Adaptive control of mechanical impedance by coactivation of antagonist muscles. *IEEE Trans. Automat. Contr.* **29**, 681–690 (1984).

Downloaded from https://www.science.org at The Hong Kong University of Science and Technology (Guangzhou) on May 25, 2026

39. N. Hogan, Impedance control: An approach to manipulation, in *1984 American Control Conference* (IEEE, 1984), pp. 304–313.
40. N. Hogan, Impedance control: An approach to manipulation: Part II—Implementation. *J. Dyn. Syst. Meas. Control* **107**, 8–16 (1985).
41. P. Song, Y. Yu, X. Zhang, A tutorial survey and comparison of impedance control on robotic manipulation. *Robotica* **37**, 801–836 (2019).
42. F. J. Abu-Dakka, M. Saveriano, Variable impedance control and learning—A review. *Front. Robot. AI* **7**, 590681 (2020).
43. S. Jung, T. C. Hsia, R. G. Bonitz, Force tracking impedance control of robot manipulators under unknown environment. *IEEE Trans. Control Syst. Technol.* **12**, 474–483 (2004).
44. N. Hogan, Stable execution of contact tasks using impedance control. *IEEE Int. Conf. Robot. Autom.* **4**, 1047–1054 (1987).
45. J. F. Soechting, M. Flanders, Sensorimotor control of contact force. *Curr. Opin. Neurobiol.* **18**, 565–572 (2008).
46. Ö. Ekeberg, A combined neuronal and mechanical model of fish swimming. *Biol. Cybern.* **69**, 363–374 (1993).
47. A. J. Ijspeert, J. Hallam, D. Willshaw, From lampreys to salamanders: Evolving neural controllers for swimming and walking, in *From Animals to Animats, Proceedings of the Fifth International Conference of The Society for Adaptive Behavior (SAB98)* (MIT Press, 1998), pp. 390–399.
48. R. Thandiackal, K. Melo, L. Paez, J. Herault, T. Kano, K. Akiyama, F. Boyer, D. Ryczko, A. Ishiguro, A. J. Ijspeert, Emergence of robust self-organized undulatory swimming based on local hydrodynamic force sensing. *Sci. Robot.* **6**, eabf6354 (2021).
49. C. Fitzgerald, Developing Baxter, in *2013 IEEE Conference on Technologies for Practical Robot Applications (TePRA)* (IEEE, 2013), pp. 1–6.
50. D. Marr, W. T. Thach, "A theory of cerebellar cortex" in *From the Retina to the Neocortex: Selected Papers of David Marr*, L. Vaina, Ed. (Birkhäuser, 1991), pp. 11–50.
51. J. S. Albus, A theory of cerebellar function. *Math. Biosci.* **10**, 25–61 (1971).
52. M. Ito, Neurophysiological aspects of the cerebellar motor control system. *Int. J. Neurol.* **7**, 162–176 (1970).
53. J. L. Raymond, J. F. Medina, Computational principles of supervised learning in the cerebellum. *Annu. Rev. Neurosci.* **41**, 233–253 (2018).
54. J. F. Medina, Teaching the cerebellum about reward. *Nat. Neurosci.* **22**, 846–848 (2019).
55. J. Knüsel, A. Crespi, J.-M. Cabelguen, A. J. Ijspeert, D. Ryczko, Reproducing five motor behaviors in a salamander robot with virtual muscles and a distributed CPG controller regulated by drive signals and proprioceptive feedback. *Front. Neurorobot.* **14**, 604426 (2020).
56. A. Bruel, I. Abadía, T. Collin, I. Sakr, H. Lorach, N. R. Luque, E. Ros, A. Ijspeert, The spinal cord facilitates cerebellar upper limb motor learning and control; inputs from neuromusculoskeletal simulation. *PLOS Comput. Biol.* **20**, e1011008 (2024).
57. W. Thach, Correlation of neural discharge with pattern and force of muscular activity, joint position, and direction of intended next movement in motor cortex and cerebellum. *J. Neurophysiol.* **41**, 654–676 (1978).
58. S. H. Scott, J. F. Kalaska, Reaching movements with similar hand paths but different arm orientations. I. Activity of individual cells in motor cortex. *J. Neurophysiol.* **77**, 826–852 (1997).
59. D. Humphrey, Separate cell systems in the motor cortex of the monkey for the control of joint movement and of joint stiffness. *Electroencephalogr. Clin. Neurophysiol. Suppl.* **36**, 393–408 (1982).
60. D. Humphrey, Separate cortical systems for the control of joint movement and joint stiffness: Reciprocal activation and coactivation of antagonist muscles. *Adv. Neurol.* **39**, 347–372 (1983).
61. M. L. Latash, Muscle coactivation: Definitions, mechanisms, and functions. *J. Neurophysiol.* **120**, 88–104 (2018).
62. P. L. Gribble, D. J. Ostry, Compensation for loads during arm movements using equilibrium-point control. *Exp. Brain Res.* **135**, 474–482 (2000).
63. C. Disselhorst-Klug, T. Schmitz-Rode, G. Rau, Surface electromyography and muscle force: Limits in sEMG–force relationship and new approaches for applications. *Clin. Biomech.* **24**, 225–235 (2009).
64. B. Beihoff, A survey of torque transduction methodologies for industrial applications, in *Conference Record of 1996 Annual Pulp and Paper Industry Technical Conference* (IEEE, 1996), pp. 220–229.
65. A. J. Del-Ama, Á. Gil-Agudo, J. L. Pons, J. C. Moreno, Hybrid FES-robot cooperative control of ambulatory gait rehabilitation exoskeleton. *J. Neuroeng. Rehabil.* **11**, 27 (2014).
66. J. A. Mettler, D. M. Magee, B. M. Doucet, Low-frequency electrical stimulation with variable intensity preserves torque. *J. Electromyogr. Kinesiol.* **42**, 49–56 (2018).
67. N. Royer, K. Nosaka, V. Doguet, M. Jubeau, Neuromuscular responses to isometric, concentric and eccentric contractions of the knee extensors at the same torque-time integral. *Eur. J. Appl. Physiol.* **122**, 127–139 (2022).
68. D. W. Franklin, R. Osu, E. Burdet, M. Kawato, T. E. Milner, Adaptation to stable and unstable dynamics achieved by combined impedance control and inverse dynamics model. *J. Neurophysiol.* **90**, 3270–3282 (2003).
69. R. Osu, D. W. Franklin, H. Kato, H. Gomi, K. Domen, T. Yoshioka, M. Kawato, Short-and long-term changes in joint co-contraction associated with motor learning as revealed from surface EMG. *J. Neurophysiol.* **88**, 991–1004 (2002).
70. J. B. Heald, D. W. Franklin, D. M. Wolpert, Increasing muscle co-contraction speeds up internal model acquisition during dynamic motor learning. *Sci. Rep.* **8**, 16355 (2018).
71. N. B. Wyatt, M. W. Liberatore, Rheology and viscosity scaling of the polyelectrolyte xanthan gum. *J. Appl. Polym. Sci.* **114**, 4076–4084 (2009).
72. A. De Santis, B. Siciliano, A. De Luca, A. Bicchi, An atlas of physical human–robot interaction. *Mech. Mach. Theory* **43**, 253–270 (2008).
73. F. J. Valero-Cuevas, *Fundamentals of Neuromechanics,* vol. 8 of *Biosystems & Biorobotics (BIOSYSROB),* E. Guglielmelli, Ed. (Springer, 2016).
74. T. E. Milner, Adaptation to destabilizing dynamics by means of muscle cocontraction. *Exp. Brain Res.* **143**, 406–416 (2002).
75. C. Ott, R. Mukherjee, Y. Nakamura, A hybrid system framework for unified impedance and admittance control. *J. Intell. Robot. Syst.* **78**, 359–375 (2015).
76. N. Berezny, M. Ahmadi, Interpolating across the impedance/admittance spectrum with Unified Interaction Control. *Discov. Mech. Eng.* **2**, 16 (2023).
77. F. Cavenago, L. Voli, M. Massari, Adaptive hybrid system framework for unified impedance and admittance control. *J. Intell. Robot. Syst.* **91**, 569–581 (2018).
78. D. A. Lawrence, Impedance control stability properties in common implementations, in *Proceedings. 1988 IEEE International Conference on Robotics and Automation* (IEEE, 1988), pp. 1185–1190.
79. H. N. Rahimi, I. Howard, L. Cui, Neural impedance adaption for assistive human–robot interaction. *Neurocomputing* **290**, 50–59 (2018).
80. J. Buchli, F. Stulp, E. Theodorou, S. Schaal, Learning variable impedance control. *Int. J. Robot. Res.* **30**, 820–833 (2011).
81. K. Lee, M. Buss, Force tracking impedance control with variable target stiffness. *IFAC Proc. Vol.* **41**, 6751–6756 (2008).
82. L. Muratore, A. Laurenzi, N. G. Tsagarakis, A self-modulated impedance multimodal interaction framework for human-robot collaboration, in *2019 International Conference on Robotics and Automation (ICRA)* (IEEE, 2019), pp. 4998–5004.
83. A. Ajoudani, N. Tsagarakis, A. Bicchi, Tele-impedance: Teleoperation with impedance regulation using a body–machine interface. *Int. J. Robot. Res.* **31**, 1642–1656 (2012).
84. E. L. Miller, L. Murray, L. Richards, R. D. Zorowitz, T. Bakas, P. Clark, S. A. Billinger, American Heart Association Council on Cardiovasculaer Nursing and the Stroke Council, Comprehensive overview of nursing and interdisciplinary rehabilitation care of the stroke patient: A scientific statement from the American Heart Association. *Stroke* **41**, 2402–2448 (2010).
85. S. Haddadin, E. Croft, "Physical human–robot interaction" in *Springer Handbook of Robotics*, B. Siciliano, O. Khatib, Eds. (Springer, 2016), pp. 1835–1874.
86. D. P. Ferris, M. Louie, C. T. Farley, Running in the real world: Adjusting leg stiffness for different surfaces. *Proc. R. Soc. London Ser. B Biol. Sci.* **265**, 989–994 (1998).
87. K. C. Galloway, J. E. Clark, M. Yim, D. E. Koditschek, Experimental investigations into the role of passive variable compliant legs for dynamic robotic locomotion, in *2011 IEEE International Conference on Robotics and Automation* (IEEE, 2011), pp. 1243–1249.
88. P. Ramdya, A. J. Ijspeert, The neuromechanics of animal locomotion: From biology to robotics and back. *Sci. Robot.* **8**, eadg0279 (2023).
89. M. Quigley, K. Conley, B. Gerkey, J. Faust, T. Foote, J. Leibs, R. Wheeler, A. Y. Ng, ROS: An open-source robot operating system, in *ICRA Workshop on Open Source Software* (IEEE, 2009), vol. 3, p. 5.
90. S. F. Giszter, F. A. Mussa-Ivaldi, E. Bizzi, Convergent force fields organized in the frog's spinal cord. *J. Neurosci.* **13**, 467–491 (1993).
91. A. G. Feldman, Once more on the equilibrium-point hypothesis (λ model) for motor control. *J. Mot. Behav.* **18**, 17–54 (1986).
92. D. A. Kistemaker, A. J. Van Soest, M. F. Bobbert, Is equilibrium point control feasible for fast goal-directed single-joint movements? *J. Neurophysiol.* **95**, 2898–2912 (2006).
93. E. Burdet, K. P. Tee, I. Mareels, T. E. Milner, C.-M. Chew, D. W. Franklin, R. Osu, M. Kawato, Stability and motor adaptation in human arm movements. *Biol. Cybern.* **94**, 20–32 (2006).
94. T. Buhrmann, E. A. Di Paolo, Spinal circuits can accommodate interaction torques during multijoint limb movements. *Front. Comput. Neurosci.* **8**, 144 (2014).
95. A. J. Fink, K. R. Croce, Z. J. Huang, L. Abbott, T. M. Jessell, E. Azim, Presynaptic inhibition of spinal sensory feedback ensures smooth movement. *Nature* **509**, 43–48 (2014).
96. D. J. Bennett, Stretch reflex responses in the human elbow joint during a voluntary movement. *J. Physiol.* **474**, 339–351 (1994).
97. J. Shemmell, M. A. Krutky, E. J. Perreault, Stretch sensitive reflexes as an adaptive mechanism for maintaining limb stability. *Clin. Neurophysiol.* **121**, 1680–1689 (2010).
98. M. Ito, Cerebellar microcomplexes. *Int. Rev. Neurobiol.* **41**, 475–487 (1997).
99. R. R. Carrillo, F. Naveros, E. Ros, N. R. Luque, A metric for evaluating neural input representation in supervised learning networks. *Front. Neurosci.* **12**, 913 (2018).
100. W. Gerstner, W. M. Kistler, *Spiking Neuron Models: Single Neurons, Populations, Plasticity* (Cambridge Univ. Press, 2002).

Downloaded from https://www.science.org at The Hong Kong University of Science and Technology (Guangzhou) on May 25, 2026

101. G. A. Pratt, M. M. Williamson, Series elastic actuators, in *Proceedings 1995 IEEE/RSJ International Conference on Intelligent Robots and Systems. Human Robot Interaction and Cooperative Robots* (IEEE, 1995), vol. 1, pp. 399–406.
102. S. Cremer, L. Mastromoro, D. O. Popa, On the performance of the Baxter research robot, in *2016 IEEE International Symposium on Assembly and Manufacturing (ISAM)* (IEEE, 2016), pp. 106–111.
103. M. Alqatamin, N. Taghavi, S. K. Das, D. O. Popa, Observer-free output feedback tracking control for collaborative robotics, in *2022 IEEE 18th International Conference on Automation Science and Engineering (CASE)* (IEEE, 2022), pp. 1017–1022.
104. P. van der Smagt, Benchmarking cerebellar control. *Robot. Auton. Syst.* **32**, 237–251 (2000).
105. H. Hoffmann, G. Petkos, S. Bitzer, S. Vijayakumar, Sensor-assisted adaptive motor control under continuously varying context, in *Proceedings of the Fourth International Conference on Informatics in Control, Automation and Robotics, Intelligent Control Systems and Optimization (ICINCO-ICSO*) (INSTICC, 2007), pp. 262–269.
106. S. Van der Walt, J. L. Schönberger, J. Nunez-Iglesias, F. Boulogne, J. D. Warner, N. Yager, E. Gouillart, T. Yu, scikit-image: Image processing in Python. *PeerJ* **2**, e453 (2014).
107. B. L. Welch, The generalization of "STUDENT'S" problem when several different population varlances are involved. *Biometrika* **34**, 28–35 (1947).
108. P. Virtanen, R. Gommers, T. E. Oliphant, M. Haberland, T. Reddy, D. Cournapeau, E. Burovski, P. Peterson, W. Weckesser, J. Bright, SciPy 1.0: Fundamental algorithms for scientific computing in Python. *Nat. Methods* **17**, 261–272 (2020).
109. E. Ros, R. Carrillo, E. M. Ortigosa, B. Barbour, R. Agís, Event-driven simulation scheme for spiking neural networks using lookup tables to characterize neuronal dynamics. *Neural Comput.* **18**, 2959–2993 (2006).
110. N. R. Luque, F. Naveros, R. R. Carrillo, E. Ros, A. Arleo, Spike burst-pause dynamics of Purkinje cells regulate sensorimotor adaptation. *PLOS Comput. Biol.* **15**, e1006298 (2019).
111. S. Kuroda, K. Yamamoto, H. Miyamoto, K. Doya, M. Kawato, Statistical characteristics of climbing fiber spikes necessary for efficient cerebellar learning. *Biol. Cybern.* **84**, 183–192 (2001).
112. J. Keating, W. Thach, Nonclock behavior of inferior olive neurons: Interspike interval of Purkinje cell complex spike discharge in the awake behaving monkey is random. *J. Neurophysiol.* **73**, 1329–1340 (1995).
113. N. R. Luque, J. A. Garrido, R. R. Carrillo, J.-M. C. Olivier, E. Ros, Cerebellarlike corrective model inference engine for manipulation tasks. *IEEE Trans. Syst. Man Cybern. B Cybern.* **41**, 1299–1312 (2011).
114. C. Boucheny, R. Carrillo, E. Ros, O. J.-M. Coenen, Real-time spiking neural network: An adaptive cerebellar model, in *International Work-Conference on Artificial Neural Networks* (Springer, 2005), pp. 136–144.

Acknowledgments: We thank L. Paez for the valuable discussions regarding the muscle model. We thank M. T. López-López and F. J. Vázquez-Pérez for the help and assistance on viscosity measurements. We thank Y. Morel for encouraging this collaborative work and the coordination efforts during the Human Brain Project. **Funding:** This work was supported by MUSCLEBOT (CNS2022-135243) funded by MCIN/AEI/10.13039/501100011033/ and by NextGenerationEU/PRTR; TREMBLE-ICED (PID2023-146392NB-I00) funded by MCIN/AEI/10.13039/; DLROB (TED2021-131294B-I00) funded by MCIN/AEI/10.13039/501100011033/ and by NextGenerationEU/PRTR awarded to N.R.L. Additional funding was through SENSCOMP (PID2022-140095NB-I00) funded by MCIN/AEI/10.13039/501100011033/ and EU FEDER; INTARE (TED2021-131466B-I00) funded by MCIN/AEI/10.13039/501100011033/ and NextGenerationEU/PRTR awarded to E.R. This work was also supported by EU Human Brain Project Specific Grant Agreement 3 (H2020-RIA. 945539) awarded to A.I. and E.R. **Author contributions:** I.A., A.B., A.I., E.R., and N.R.L. conceived the working hypothesis, proposed approach, and experimental setup. I.A., A.B., and N.R.L. implemented the proposed approach. I.A. and N.R.L. conducted and extracted experimental results. A.I., E.R., and N.R.L. provided funding. G.C., A.I., E.R., and N.R.L. supervised this work. All authors contributed to the writing of the manuscript. **Competing interests:** The authors declare that they have no competing interests. **Data and materials availability:** All data needed to evaluate the conclusions in the paper are present in the paper or the Supplementary Materials. The dataset (https://doi.org/10.5281/zenodo.14283696) and source code (https://doi.org/10.5281/zenodo.14283645) are available at Zenodo.

Submitted 14 March 2024
Accepted 16 December 2024
Published 22 January 2025
10.1126/scirobotics.adp2356

Downloaded from https://www.science.org at The Hong Kong University of Science and Technology (Guangzhou) on May 25, 2026

Science Robotics

A neuromechanics solution for adjustable robot compliance and accuracy

Ignacio Abadía, Alice Bruel, Grégoire Courtine, Auke J. Ijspeert, Eduardo Ros, and Niceto R. Luque

Sci. Robot. **10** (98), eadp2356. DOI: 10.1126/scirobotics.adp2356

View the article online
https://www.science.org/doi/10.1126/scirobotics.adp2356
Permissions
https://www.science.org/help/reprints-and-permissions

Downloaded from https://www.science.org at The Hong Kong University of Science and Technology (Guangzhou) on May 25, 2026

Use of this article is subject to the Terms of service

Science Robotics (ISSN 2470-9476) is published by the American Association for the Advancement of Science. 1200 New York Avenue NW, Washington, DC 20005. The title *Science Robotics* is a registered trademark of AAAS.

Copyright © 2025 The Authors, some rights reserved; exclusive licensee American Association for the Advancement of Science. No claim to original U.S. Government Works